

Detecting climate signals using explainable AI with single-forcing large ensembles

Zachary M. Labe¹ and Elizabeth A. Barnes¹

¹Department of Atmospheric Science, Colorado State University, Fort Collins, CO, USA

Key Points:

- Using explainable AI methods with artificial neural networks (ANN) reveals climate patterns in large ensemble simulations
- Predictions from an ANN trained using a large ensemble without time-evolving aerosols show the highest correlation with actual observations
- A metric is proposed for quantifying the uncertainty of an ANN visualization method that extracts signals from different external forcings

Abstract

It remains difficult to disentangle the relative influences of aerosols and greenhouse gases on regional surface temperature trends in the context of global climate change. To address this issue, we use a new collection of initial-condition large ensembles from the Community Earth System Model version 1 that are prescribed with different combinations of industrial aerosol and greenhouse gas forcing. To compare the climate response to these external forcings, we adopt an artificial neural network (ANN) architecture from previous work that predicts the year by training on maps of near-surface temperature. We then utilize layer-wise relevance propagation (LRP) to visualize the regional temperature signals that are important for the ANN's prediction in each climate model experiment. To mask noise when extracting only the most robust climate patterns from LRP, we introduce a simple uncertainty metric that can be adopted to other explainable artificial intelligence (AI) problems. We find that the North Atlantic, Southern Ocean, and Southeast Asia are key regions of importance for the neural network to make its prediction, especially prior to the early-21st century. Notably, we also find that the ANN predictions based on maps of observations correlate higher to the actual year after training on the large ensemble experiment with industrial aerosols held fixed to 1920 levels. This work illustrates the sensitivity of regional temperature signals to changes in aerosol forcing in historical simulations. By using explainable AI methods, we have the opportunity to improve our understanding of (non)linear combinations of anthropogenic forcings in state-of-the-art global climate models.

Plain Language Summary

Using a machine learning method called artificial neural networks, we explore how human-caused climate drivers can affect regional patterns of surface temperature. Here we use a climate model with different combinations of greenhouse gases and industrial aerosols (particles in the atmosphere) to understand their influence on climate change and variability. By employing visualization tools to see how the artificial neural network makes its predictions, we can better recognize how these climate drivers influence global temperature in the past, present, and future. For instance, we find that aerosols emitted in the 20th century and early 21st century have influenced global warming temperature trends in some areas of the world, such as over the North Atlantic Ocean. Machine learning accompanied by new visualization methods have the potential to bring new in-

sights into understanding the effects of global climate change in observations and models.

1 Introductions

Separating human-induced climate forcing from internal variability remains a key challenge for attributing and communicating the impacts of global climate change on regional scales. While state-of-the-art global climate models (GCMs) include anthropogenic (e.g., greenhouse gases and aerosols) and natural (e.g., volcanoes) radiative forcings, it remains difficult to understand their combined interactions and associated effects on climate variability (Stocker et al., 2013). The chaotic noise of the atmosphere (internal variability) also gives rise to additional uncertainties on seasonal to multi-decadal timescales (Deser et al., 2012; Kay et al., 2015). Moreover, it still is difficult to constrain and reduce the uncertainty in Earth’s equilibrium climate sensitivity over the historical period (Sherwood et al., 2020). The complex interactions between internal and external climate forcings make it challenging to interpret the physical mechanisms driving regional and even global-scale temperature variability (Stott et al., 2006; Knutti et al., 2010; Maher et al., 2014; D. M. Smith et al., 2016; Medhaug et al., 2017; Hausteine et al., 2019; Mankin et al., 2020).

While greenhouse gas forcing dominates the overall climate change signal (net warming), an abundance of anthropogenic aerosols can also influence Earth’s surface temperature (net cooling) by scattering or absorbing incoming solar radiation (Bellouin et al., 2020). Further, recent studies have found an influence of anthropogenic aerosols on tropospheric temperatures (e.g., Santer et al., 2019; Mitchell et al., 2020), oceanic internal variability (e.g., Hausteine et al., 2019; Dagan et al., 2020; Meehl, Hu, et al., 2020; Qin et al., 2020), the hydrologic cycle (e.g., Marvel et al., 2019; Bonfils et al., 2020), and the large-scale atmospheric circulation (e.g., Allen & Sherwood, 2011; Wang et al., 2020). Meanwhile, less attention has been given to comparing regional climate trends to individual anthropogenic external forcings relative to the influence of internal variability (see examples by Polvani et al., 2011; Santer et al., 2019; Bonfils et al., 2020; Chemke et al., 2020; Deser, Phillips, et al., 2020). For instance, after using an initial-condition large ensemble, Oudar et al. (2018) found a larger role for internal variability than suggested by earlier Coupled Model Intercomparison Project Phase 5 (CMIP5) studies (e.g., D. M. Smith

75 et al., 2016) when attributing the impact of anthropogenic aerosols to the global mean
76 surface temperature trend in the early 21st century.

77 In addition to the influence of internal variability, the effective radiative forcing from
78 anthropogenic aerosol emissions also remains uncertain over the historical period (Booth
79 et al., 2018; Bellouin et al., 2020; Thorsen et al., 2020). In a novel experiment design,
80 Dittus et al. (2020) assessed the sensitivity of a climate model to a plausible range of his-
81 torical aerosol forcings. They found better agreement between the observed global mean
82 surface temperature record and an experiment with smaller net aerosol forcing than the
83 standard configuration of the GCM. Consequently, this suggests that temperature sig-
84 nals may be highly sensitive to small changes in aerosols, even when the aerosol forcing
85 in GCMs is constrained to fall within observational estimates (Dittus et al., 2020). This
86 also could be one explanation for the higher climate sensitivities found in CMIP6 mod-
87 els (Flynn & Mauritsen, 2020; Meehl, Senior, et al., 2020).

88 Recent advances in computational power have led to the development of a grow-
89 ing number of initial-condition large ensembles for assessing climate change and variabil-
90 ity (Deser, Lehner, et al., 2020; Deser, 2020). Within a single large ensemble GCM sim-
91 ulation, one can obtain the forced response (i.e., climate signal) by averaging across in-
92 dividual ensemble members that differ by only a small random perturbation error. Thus,
93 if the model is correct, observations of the real world should fall within the ensemble spread
94 in order to reflect both a common forced signal (climate change) and the unpredictable
95 noise of the atmosphere. In other words, the statistical characteristics of internal vari-
96 ability should be similar between the real world and the individual model ensemble mem-
97 bers. However, although numerous statistical methods have been proposed to further ex-
98 tract the forced response from internal variability (e.g., Hegerl et al., 1996; Deser et al.,
99 2016; Barnes et al., 2019; Santer et al., 2019; Sippel et al., 2019; Barnes et al., 2020; Sip-
100 ppel et al., 2020; Wills, Battisti, et al., 2020), the problem of climate pattern attribution
101 still remains difficult (Wills, Sippel, & Barnes, 2020).

102 To improve our understanding of the forced signals from individual anthropogenic
103 climate drivers amidst the noise of internal variability, we implement a method of ex-
104 plainable artificial intelligence (XAI) using data from a novel set of single-forcing large
105 ensemble experiments. The adoption of machine learning applications for geoscience is-
106 sues continues to rapidly grow (Ebert-Uphoff et al., 2019; McGovern et al., 2019; Rasu

107 et al., 2019; Boukabara et al., 2020; Toms et al., 2020; Watson-Parris, 2020), especially
108 due to an increasing number of XAI methods (Samek et al., 2017; Montavon et al., 2018;
109 Samek et al., 2020). Recently, machine learning models have been used for diverse ap-
110 plications in mesoscale meteorology (e.g., Gagne et al., 2019; Lagerquist et al., 2020),
111 numerical weather prediction (e.g., Rasp et al., 2020; Weyn et al., 2020), simulating cloud
112 and radiation processes in GCMs (e.g., Rasp et al., 2018), turbulence and convection pa-
113 rameterizations (e.g., Beucler et al., 2019; Zanna & Bolton, 2020), attribution of global
114 climate change (e.g., Barnes et al., 2019; Mansfield et al., 2020; Sippel et al., 2020), and
115 reconstructions of historical temperature trends (Kadow et al., 2020). To explore how
116 machine learning models are making their predictions, we focus on using XAI techniques
117 in order to gain new scientific insights for climate science.

118 In this study, we use artificial neural networks (ANN) in association with an ex-
119 plainability method called layer-wise relevance propagation (LRP) on data from climate
120 model simulations. By comparing the LRP results between ANNs, we compare climate
121 patterns that are related to different combinations of external forcings, namely, green-
122 house gases and industrial aerosols. Finally, we assess the utility of the ANNs by eval-
123 uating them on real world observations and introduce a metric to mask noise in assess-
124 ing the LRP visualizations.

125 **2 Data and Methods**

126 **2.1 Climate Model Simulations**

127 For all climate model data, we use large ensemble simulations performed by the Com-
128 munity Earth System Model version 1 (CESM1; Hurrell et al., 2013) covering 1920 to
129 2080. CESM1 is a fully coupled GCM and is run with 30 vertical levels and a horizon-
130 tal resolution of 1° . The atmospheric model is the Community Atmosphere Model ver-
131 sion 5 (CAM5; Neale et al., 2012), which is coupled to interactive land, ocean, and sea
132 ice components.

133 Here, we first analyze the widely-used 40-member large ensemble as described in
134 Kay et al. (2015), which we refer to as “ALL” (for all-forcing). The large number of en-
135 semble members is useful for characterizing atmospheric internal variability (or noise)
136 in the climate system (Maher et al., 2019; Deser, Lehner, et al., 2020). Each of the en-
137 semble members have the same external forcing, but are generated from a small random

138 round-off difference in the atmospheric initial conditions. Historical forcing is imposed
139 from 1920 to 2005, and thereafter Representative Concentration Pathway 8.5 (RCP8.5;
140 Vuuren et al., 2011) is used to simulate a worst-case climate scenario through the end
141 of the 21st century (Peters & Hausfather, 2020). Land use/land cover changes, biomass
142 burning, and stratospheric ozone concentrations also evolve with time in the ALL sim-
143 ulation. Although large uncertainties exist, CESM1’s total aerosol effective radiative forc-
144 ing falls within one standard deviation of observational evidence (Zelinka et al., 2014;
145 Bellouin et al., 2020; Deser, Phillips, et al., 2020). We will return to this last point later
146 in the study.

147 In addition, we also use a set of two new single-forcing simulations from CESM1
148 that are both run with 20 ensemble members (Deser, Phillips, et al., 2020). These large
149 ensembles have the same GCM, initialization protocol, and external forcing as ALL, but
150 differ by one time-evolving forcing agent that is withheld per simulation. In particular,
151 greenhouse gas concentrations are held fixed to 1920 levels in one experiment (AER+),
152 and industrial aerosols are held fixed to 1920 levels in another (GHG+). While our no-
153 tation in this study reflects the dominant external forcing agent per simulation (either
154 greenhouse gases (GHG) or industrial aerosols (AER)), we do note that there are other
155 important climate feedbacks and natural variability included in each experiment (hence,
156 the “+” sign) that may contribute to our interpretation of the ANN results (e.g., Luys-
157 saert et al., 2014; Hawkins et al., 2017; Deng et al., 2020; Lehner et al., 2020; Maher et
158 al., 2020; Milinski et al., 2020). Since we only focus on one GCM (CESM1) with histor-
159 ical and RCP8.5 forcing, differences between the simulations cannot be due to emission
160 scenario uncertainties or model structural uncertainties that would arise from using, for
161 instance, CMIP5/6 (Hawkins & Sutton, 2009; Knutti & Sedlacek, 2013; Lehner et al.,
162 2020).

163 After taking into account the smaller ensemble size of the single-forcing runs, we
164 only consider the first 20 members of ALL. However, this does not affect the skill of the
165 ANN for training and testing data (not shown). We apply a bilinear interpolation to the
166 three sets of large ensembles so that they share a slightly coarser latitude by longitude
167 global grid ($1.9^\circ \times 2.5^\circ$). We only consider fields of monthly near-surface air tempera-
168 ture (TREFHT; $^\circ\text{C}$) to calculate seasonal and annuals means from model output. An
169 overview of the climate model simulations used in this study can be found in Table S1.

2.2 Observations

To understand the effect of training on climate model simulations with different external forcing, we test the ANN on observations using the new National Oceanic and Atmospheric Administration/Cooperative Institute for Research in Environmental Sciences/Department of Energy (NOAA-CIRES-DOE) Twentieth Century Reanalysis (20CR) version 3 (20CRv3; also referred to here as ‘observations’) (Slivinski et al., 2019). Updates to 20CRv3 include an 80-member ensemble size for confidence estimation, a four-dimensional incremental analysis data assimilation scheme (4DIAU), and a higher resolution (T254) core model (described in Slivinski et al., 2019). These improvements lead to a reduction in biases of near-surface temperature, sea surface temperature, and sea level pressure compared to older versions of 20CR, especially in the early to mid-20th century (Compo et al., 2011; Giese et al., 2016). Further, 20CRv3 was found to be in close agreement with other independently derived reanalysis data sets, including the European Centre for Medium-Range Weather Forecasts (ECMWF) ERA-20C and CERA-20C (Slivinski et al., 2019, 2020).

We analyze monthly fields of 2-m air temperatures ($^{\circ}\text{C}$) from 20CRv3 after interpolating (bilinear) onto a common grid of 1.9° latitude by 2.5° longitude for consistency with the climate model simulations. 20CRv3 was selected for our analysis due to its temporally and spatially complete fields of 2-m temperature that are available globally from 1920 to 2015. Similar results were also obtained from the ANN after evaluating on the ECMWF ERA5 reanalysis (Hersbach et al., 2020) for the more recent 1979 to 2019 period. However, in this study, we focus our attention on 20CRv3 for consistency with the historical climate model output. A summary of the observations can be found in Table S2.

2.3 Neural Network Framework

In this analysis, we adopt a neural network architecture that was first introduced in Barnes et al. (2020) and is further illustrated here in Figure 1. We compare the impact of time-evolving greenhouse gases and industrial aerosols on a classification task of predicting the decade (year) from input maps of temperature. Each unit of the ANN input layer represents one grid point from a 2-m temperature map (13824 units per map

with dimensions of 96 latitudes by 144 longitudes), and our output layer represents the probabilities of a particular decade class (e.g., 2000-2009).

Our ANN is set up with two hidden layers that each contain 20 hidden units (relatively shallow). We find that increasing the number of layers does not improve the skill of the model (Figure S1), and this architecture supports the interpretability of the fully connected neural network for scientific discovery. In particular, we apply the Rectified Linear Unit (ReLU; Agarap, 2018) activation function to all hidden layer nodes before the output layer, which is defined as $f(x) = \max(0, x)$. ReLU is well equipped for use in LRP visualization, since it tests whether individual neurons have been activated (Toms et al., 2020). We also apply a soft-max function to the output layer, which remaps the decadal class probabilities so that they add up to one. Both ReLU and soft-max functions are common in ANN classification problems such as ours (e.g., Lecun et al., 2015; Goodfellow et al., 2016; Samek et al., 2020).

To retrieve the predicted year (output) by the ANN from the maps of 2-m temperature (input), we use a method called fuzzy classification encoding and decoding (Zadeh, 1965; Amo et al., 2004). This occurs during the ANN’s output layer (see Barnes et al. (2020)). From this approach, each decade is identified by its central year (e.g., 2005 for 2000 to 2009). The ANN is then designed to assign an input map to the probability of it falling under a particular decade class (encode). Finally, fuzzy classification determines the particular year by computing the weighted sum of the decadal class probabilities (decode). For instance, the year 2008 would be encoded with the probability of 0.7 of belonging to class center 2005 (for 2000 to 2009) and 0.3 of belonging to class center 2015 (for 2010 to 2019). Thus, we can compute the exact year as follows: $0.7 \cdot 2005 + 0.3 \cdot 2015 = 2008$. Additional examples are depicted in Figure 2 of Barnes et al. (2020). Given our approach using both LRP and fuzzy classification, we do not explore the more typical method of multiple linear regression in this work. However, that approach has been explored in Barnes et al. (2019, 2020) for CMIP temperature and precipitation data.

Before the maps are fed into the ANN, all training data are standardized by their standard deviation across all ensemble members and years at each grid point. Each ANN is then trained using a randomly selected subset of 80% of the climate model simulation data (16 ensemble members) and tested on the remaining 20% (4 ensemble members). During training, our loss function uses binary cross-entropy/log loss, which acts to pe-

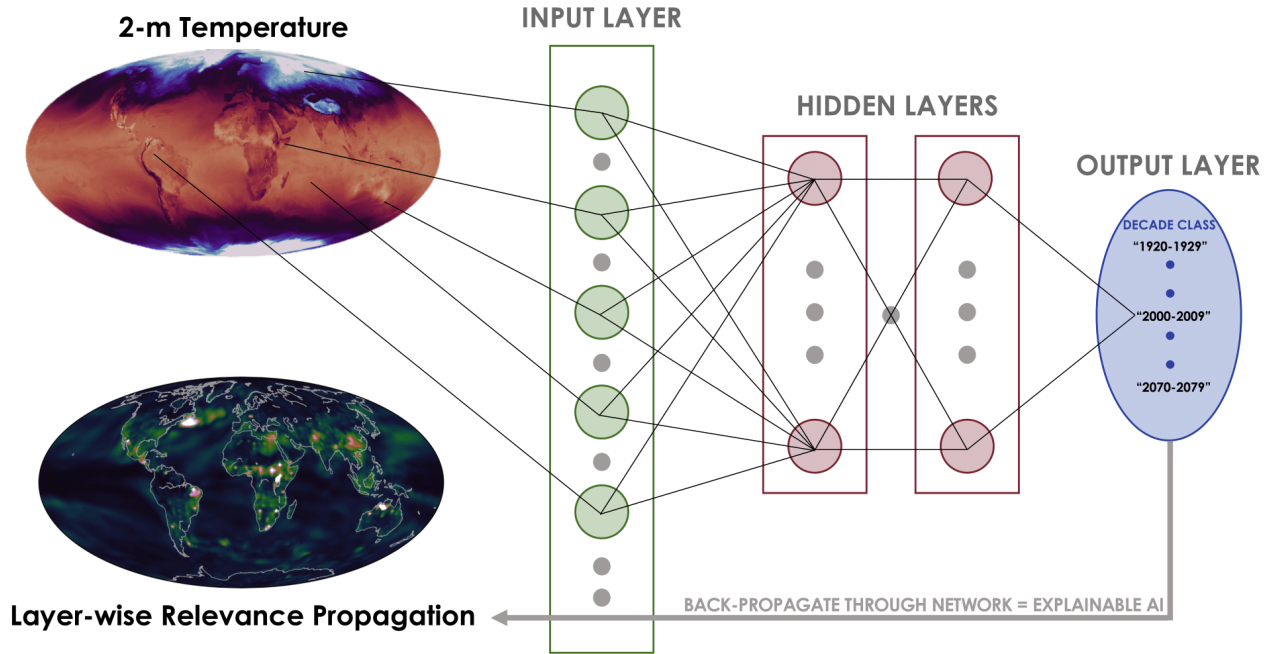


Figure 1. Schematic of the artificial neural network (ANN) used in this study for predicting the decade/year from global maps of 2-m air temperature (input layer). The shallow ANN features two hidden layers that both contain 20 hidden units. The output layer uses fuzzy classification (Zadeh, 1965) to assign each prediction year to the probability of it occurring in a single decade (e.g., within 2000-2009) (Barnes et al., 2020). An example heatmap using layer-wise relevance propagation (LRP; Bach et al., 2015) is also illustrated here. LRP highlights the regions of greater relevance for the ANN to predict the year by propagating an output sample backward through the frozen nodes of the ANN until it reaches the input layer (Toms et al., 2020).

232 nalyze the ANN when the prediction is wrong, but the model confidence is still high. The
233 ANN are trained using the Nesterov method (momentum = 0.9) for stochastic gradient
234 descent (SGD; Ruder, 2016) for 500 epochs. While the interpretability results are not
235 sensitive to our selection in hyperparameters, we set our learning rate to 0.01 and a batch
236 size to 32 for each ANN used to generate the following figures.

237 To overcome the problem of overfitting the input data, we use L_2 ridge regulariza-
238 tion (Friedman, 2012). The L_2 parameter is set to 0.01 and applied to the weights of the
239 first hidden layer. L_2 regularization imposes a penalty on the model by adding a coef-
240 ficient to the loss function that is proportional to the sum of the squares of the feature
241 weights. Thus, L_2 regularization leads to weights that are more smoothly distributed across
242 the model and are not as sensitive to outliers in the input data. Importantly, and in re-
243 lation to standard climate science tools, the inclusion of this parameter accounts for spa-
244 tial autocorrelation that can exist in the 2-m temperature fields. L_2 also improves the
245 interpretation of the LRP heatmaps for identifying key regions that are relevant for the
246 ANN to make its prediction (e.g., see Figure 3 in Barnes et al., 2020).

247 **2.4 Layer-wise Relevance Propagation**

248 The motivation for this work is to reveal the underlying climate patterns that are
249 learned by the ANN from climate model simulations with different combinations of ex-
250 ternal forcing. As we will show, using XAI tools alongside existing climate science meth-
251 ods have the potential to bring new insights for interpreting projections of climate change
252 in GCMs.

253 For this work, we use an interpretation method called LRP (Bach et al., 2015; Mon-
254 tavon et al., 2018) for tracing the decisions determined by the ANN. While there are an
255 increasing number of LRP routines, we use a form here (alpha-beta rule) that works well
256 for ReLU networks and is related to Taylor series expansion (Montavon et al., 2017). By
257 propagating information backward until the first layer of the ANN is reached, we learn
258 about the individual input units (features) that are “relevant” to make the ANN’s pre-
259 diction.

260 While a detailed overview of using LRP in the geosciences is provided in Toms et
261 al. (2020), we briefly describe the method here: (1) the weights and biases of the ANN
262 are frozen after training, (2) a single prediction output (prior to the soft-max function)

263 is conserved and propagated backward through each node of the ANN based on the frozen
 264 weights and biases, (3) the feature relevance is learned until the propagation reaches the
 265 input layer, and (4) the final output of LRP retains the original dimensions of the in-
 266 put data by showing the relevance for each pixel (i.e., gridded latitude by longitude points
 267 on a map). This process is repeated for every sample. Hence, we are left with a spatial
 268 heatmap (unitless) showing the regions of importance for the ANN to determine the decade
 269 (see Figure 1).

270 In this study, our heatmaps are composites of both training and testing sample data,
 271 because we are interested in where the ANN is learning regional indicators to make all
 272 predictions. However, our LRP results are nearly the same when only using a compos-
 273 ite of testing data (e.g., Figure S13). Since our output layer can return multiple prob-
 274 abilities of a 2-m temperature map occurring in a particular decade (fuzzy classification
 275 encoding and decoding), we only propagate the output value with the highest probabili-
 276 ty of belonging to a particular decade. Again, LRP can only propagate one single out-
 277 put node backwards at a time. However, previous work has found that this does not af-
 278 fect the interpretation of the LRP output (Barnes et al., 2020). One final note about our
 279 use of LRP is that it returns information that positively contributes to the ANN’s pre-
 280 dicted likelihood (i.e., increases confidence in the prediction). Other XAI methods ex-
 281 plore ways to interpret contributions that lead to less confident predictions (e.g., Botari
 282 et al., 2020), but that is beyond the scope of this analysis. To interpret the heatmap fig-
 283 ures in this study, the higher relevance values indicate greater importance for the ANN’s
 284 prediction. Lastly, we introduce a method to mask noise (i.e., relevance) in the LRP out-
 285 put (Section 3.2).

286 **3 Results**

287 **3.1 Response to External Forcing**

288 *3.1.1 Evolution of simulated and observed trends*

289 We first evaluate the three large ensemble experiments (AER+, GHG+, ALL) us-
 290 ing more traditional climate science methods (i.e., trend analysis, signal-to-noise ratios,
 291 and timing of emergence) to understand the spatial patterns of the 2-m temperature re-
 292 sponse. Figure 2 shows annual maps of temperature trends over four separate 40-year
 293 periods for the ensemble mean of each experiment. In the historical period, there is an

294 observed cooling for AER+ (time-evolving aerosols; constant greenhouse gases) for all
295 continental regions and most of the world’s oceans (Figures 2a-2b). However, there is
296 a notable statistically significant region of warming over parts of the North Atlantic and
297 Southern Ocean (Figure 2b). These areas of warming may be connected to a strength-
298 ened Atlantic Meridional Overturning Circulation (AMOC) (Dagan et al., 2020; Keil et
299 al., 2020; Menary et al., 2020). The global signature of cooling prior to 2000 is associ-
300 ated with an increase in industrial aerosol emissions. Trends in aerosol optical depth are
301 driven by an increase in emissions over Southeast Asia, North America, and Europe in
302 the first half of the 20th century (see Figure 2 in Deser, Phillips, et al., 2020). However,
303 a decrease in aerosol optical depth is observed in North America and Europe closer to
304 present-day with the largest aerosol forcing remaining over Southeast Asia. As indus-
305 trial aerosols are reduced over the 21st century, there is a net warming trend globally
306 in AER+ through 2080 (Figure 2c-2d). Notably, the temperature trend in the North At-
307 lantic reverses and resembles the “North Atlantic Warming Hole.” In agreement with
308 earlier studies (e.g., Dagan et al., 2020), this suggests an important role for aerosols in
309 North Atlantic climate variability. Figure 2e-2h reveals the global warming signature due
310 to the dominant greenhouse gas forcing in GHG+ (time-evolving greenhouse gases; con-
311 stant aerosols), along with a cooling patch in the North Atlantic. Relative to GHG+,
312 statistically significant warming trends emerge later in ALL (Figure 2i), which is due to
313 its greater aerosol forcing prior to 1960 (net cooling effect). As trends in optical aerosol
314 depth decrease by 2040, there are larger global temperature trends in ALL (Figure 2l)
315 compared to GHG+ (Figure 2h).

316 We compare the simulated temperature trends with observations by showing the
317 observed (using 20CRv3) 2-m temperature trend (annual mean) for two 40-year peri-
318 ods in Figure S3. However, the observations only reflect one possible realization of in-
319 ternal variability combined with the forced response. Therefore, they are not directly com-
320 parable with the ensemble mean trends presented in Figure 2. Regardless, we still find
321 some common temperature signatures emerge. By the second half of the 20th century
322 (Figure S3b), we find statistically significant warming across the majority of the trop-
323 ics and parts of North America. We also find the cooling trend over the North Atlantic
324 detectable in observations for the 1960 to 1999 period.

325 To understand the patterns of forced climate signals, we compute signal-to-noise
326 (SNR) maps in Figure S4. Here, the SNR is computed as the absolute ensemble mean

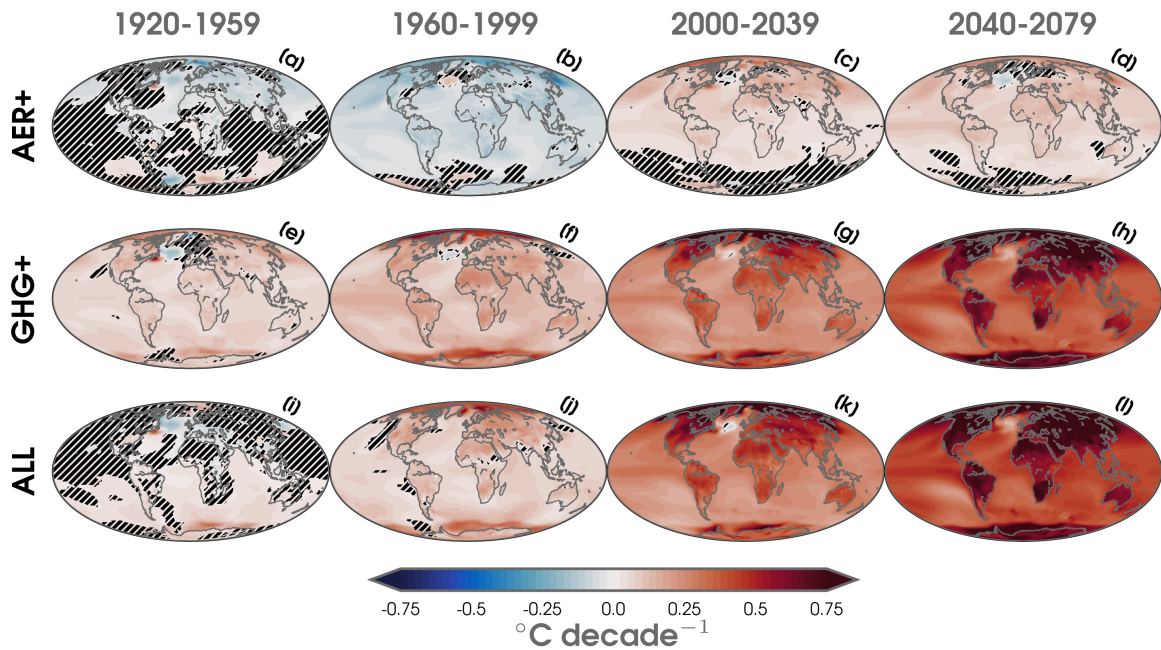


Figure 2. Annual linear least squares trends of 2-m temperature ($^{\circ}\text{C}$ per decade) over 1920 to 1959 (a,e,i), 1960 to 1999 (b,f,j), 2000 to 2039 (c,g,k), and 2040 to 2079 (d,h,l) for the ensemble means of three climate model simulations (AER+; a-d, GHG+; e-h, ALL; i-l). Statistically significant trends are shown with shaded contours at the 95% confidence level following the Mann-Kendall (MK) test (Mann, 1945; Bevan & Kendall, 1971), while those that are not are masked out using black hatch marks.

327 trend divided by the standard deviation of the individual ensemble member trends for
 328 each 40-year period. We observe the highest SNR in the tropics, which is a result of the
 329 smaller internal variability in this region. High values of SNR (> 3) emerge as early as
 330 the 1920 to 1959 period in GHG+ from the Amazon to the Indian Ocean (Figure 4e),
 331 but do not appear until the later half of the 20th century in ALL (Figure S4j-S4k). SNR
 332 values are also high in the tropics for the AER+ simulation, but there is little to no forced
 333 response (SNR < 1) in the extratropics and polar regions (Figure S4a-S4d). This is likely
 334 a result of the small temperature trends in AER+ (compared to GHG+ and ALL), which
 335 make up a small fraction of internal variability at higher latitudes. While the global warm-
 336 ing signal overwhelms internal variability in GHG+ and ALL beginning in the 2000 to
 337 2039 period, SNR values remain lower ($\sim 1-2$) in the subpolar Atlantic.

338 The effect of aerosols has a consequential role in identifying patterns and the tem-
 339 poral evolution of forced climate signals. Figure S5 shows the timing of emergence (ToE)
 340 of annual mean temperature for each large ensemble simulation. Following Lehner et al.
 341 (2017), the maps of ToE are computed as the first year that the 10-year running-mean
 342 temperature exceeds and stays above the mean 1920-1949 reference temperature by more
 343 than two standard deviations. ToE is computed for every grid point in each ensemble
 344 member before taking the ensemble mean. While there are numerous definitions and met-
 345 rics for detecting ToE (Mahlstein et al., 2012), here we are interested in a baseline to com-
 346 pare with our interpretable ANNs. Consistent with the SNR maps, we find that ToE is
 347 delayed by nearly a decade in ALL (Figure S5c) compared to GHG+ (Figure S5b) due
 348 to the effect of aerosol masking. This is particularly found across parts of Southern Asia.
 349 The North Atlantic does not emerge in GHG+ and ALL until at least the mid-21st cen-
 350 tury. Although ToE is found to be later in AER+ (Figure S5a), this is only a result of
 351 reduced aerosol optical depth in the 21st century, since there is no time-evolving green-
 352 house gas forcing in the simulation.

353 In summary, increases in industrial aerosol loading (e.g., prior to 1960) can mask
 354 the ToE of greenhouse gas-induced warming, particularly in the extratropics. Therefore,
 355 to further compare the patterns of responses that are driven by anthropogenic climate
 356 drivers, we now turn to our interpretable ANN architecture. One advantage to using our
 357 ANN is that we can address potential nonlinearities in regional patterns that evolve over
 358 time, which would not be captured in the standard methods of trend and SNR/ToE anal-
 359 ysis that are conducted grid point by grid point.

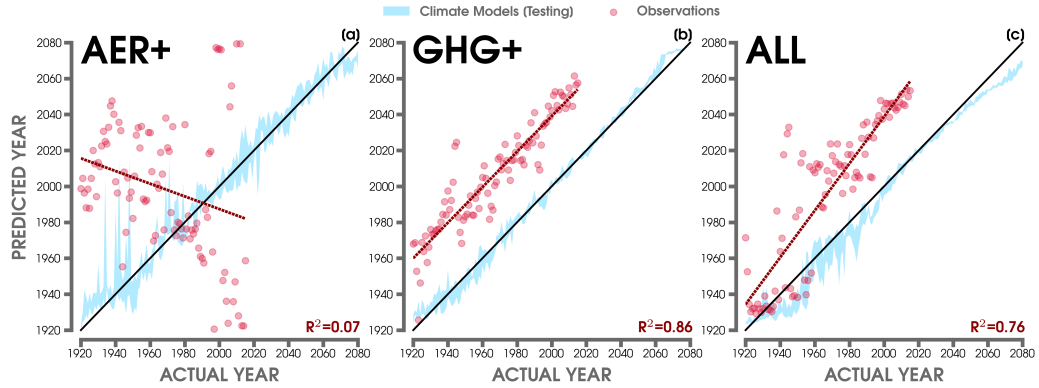


Figure 3. (a) Predictions of the year by the ANN (y-axis) compared to the actual year (x-axis) from global maps of annual 2-m temperature in AER+. (b) Same as (a) but for GHG+. (c) Same as (a) but for ALL. The blue shading highlights the 5th-95th percentiles of predictions from the large ensemble testing data. The red points show the ANN predictions using 20CRv3 observations. The red dashed line shows the linear least squares fit through the predicted observations in each model, and the associated R^2 is shown in the lower right-hand corner. The 1:1 line (or perfect prediction) is overlaid in black.

360 **3.1.2 Predictions by the ANN**

361 Figure 3 shows the predictions by the ANN after separately training and testing
 362 on each of the three large ensemble experiments. Here, we use fuzzy classification de-
 363 coding to show how well the ANN can predict the year from the input maps of 2-m tem-
 364 perature. It is clear that the ANN closely predicts the year on the climate model data
 365 (blue shading), especially after 1980 (Figure S1-S2). We also note that the ANN predicts
 366 the correct year similarly as well in AER+ compared to ALL for testing (Figure S1a,g),
 367 despite the fact that there is no time-evolving greenhouse gas forcing and consequently
 368 smaller global mean temperature trends.

369 To assess the utility of our ANNs that are trained only on climate model data, we
 370 test their performance on observations by inputting 2-m temperature maps from 20CRv3.
 371 By testing on observational data, we find striking differences between the ANN predic-
 372 tions. The ANN has no skill in predicting the year for observations after training on AER+
 373 (Figure 3a). Since the real world features a large greenhouse gas-induced warming sig-
 374 nal, the ANN does not learn regional indicators that are in common with observations.
 375 For the ANN trained on ALL, there is an improvement for predicting the order of the

376 years after 1980 (Figure 3c). Considering that a forced temperature response has not clearly
377 emerged from the background noise (see Figure S4i-S4j), we infer that this is why the
378 ANN is less able to predict the correct ordering of the years before 1980.

379 In contrast, the ANN performs quite well after training on GHG+ for predicting
380 the order of all of the years in observations (Figure 3b). Since the real world does con-
381 sist of both direct and indirect effects of greenhouse gases and aerosols, it is somewhat
382 surprising to see that the ANN trained on GHG+ has a higher correlation to the actual
383 year than for the predictions trained on ALL (Figure 4a). In fact, the observations ap-
384 proximately parallel the 1:1 line in GHG+, but are offset by about four decades. This
385 means that the patterns of forced responses are similar, but may emerge later in the cli-
386 mate model data compared to observations. This offset could also arise from a differ-
387 ence in Earth’s mean temperature that is common between climate models and reanal-
388 ysis data sets (Hawkins & Sutton, 2016). Therefore, we compare our results in Figure
389 3 to ANNs trained using input data with the global mean temperature removed from
390 each map (Figure S6). While the correlation is weaker, the overall results of the obser-
391 vations are quite similar. The ANN is still more skillful in predicting the order of the
392 years for observations on the ANN trained using GHG+. This evidence suggests that
393 the ANN is learning regional temperature signals and not just differences in the global
394 mean temperature to make its predictions, as discussed further in Section 3.3.

395 We investigate the robustness of our observational predictions in Figure 3 by us-
396 ing 100 unique ANNs trained on different combinations of training and testing data sets
397 (i.e., individual ensemble members) for six different L_2 and epoch hyperparameter choices.
398 Since L_2 regularization imposes a degree of spatial autocorrelation in the weights, we wanted
399 to see if the skill of the observational predictions could change by using different param-
400 eters for each large ensemble ANN. We then test our observational data on each of these
401 100 iterations of every ANN architecture and plot a histogram of their correlation be-
402 tween the ANN-predicted year and the actual year. Our conclusions remain the same
403 as Figure 3. We find that the median correlation is closer to 1 for GHG+ in the six ANN
404 architectures evaluated here. Figure S7 also shows a comparison between the best cor-
405 relations in GHG+ and ALL, which again confirms that the median correlation in GHG+
406 is higher than the ALL.

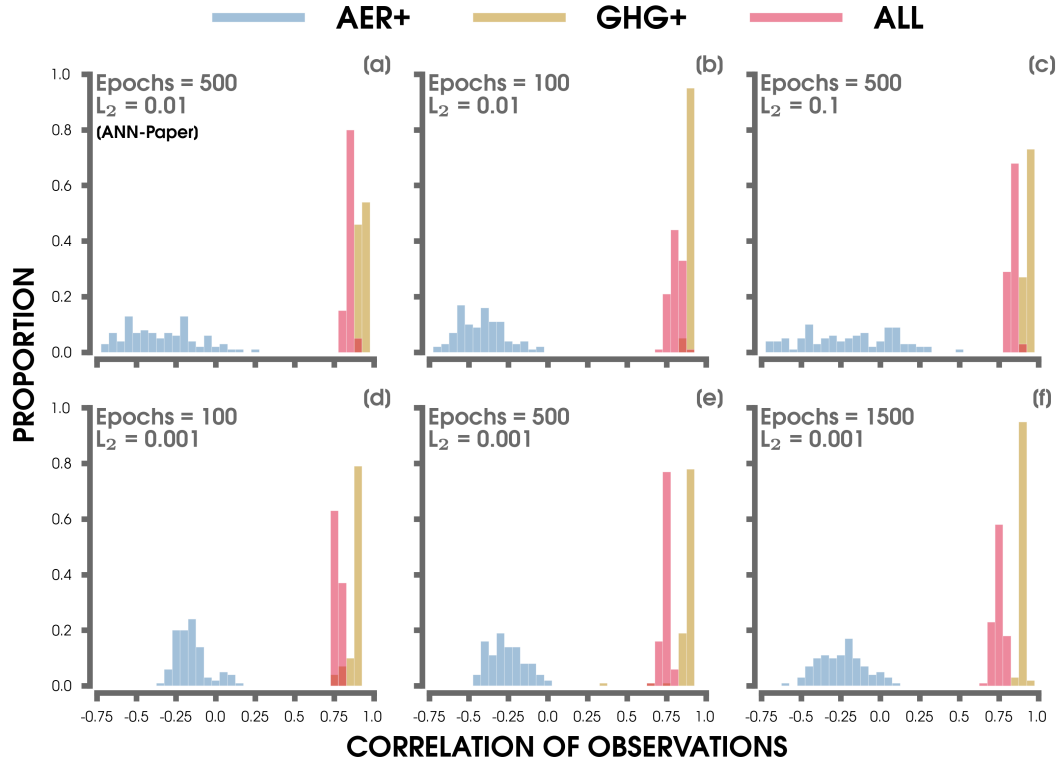


Figure 4. Histograms of the correlation between the actual years and the ANN-predicted years from 20CRv3 observations after considering 100 different combinations of training and testing data for each of the AER+ (blue), GHG+ (brown), and ALL (red) ANNs using six different combinations of epochs and L₂ regularization parameters (a-f; listed in the upper-left corner). The results from the ANN architecture used throughout the rest of the study are shown in (a).

407 Proceeding with the L_2 and epoch parameters outlined earlier (e.g., Figure 4a), we
 408 also plot a histogram of the predicted (linear) slopes for our observational data in Fig-
 409 ure S8. In agreement with our single trained ANNs in Figure 3, we find that the obser-
 410 vations tested on the ANN using GHG+ performs the closest to the 1:1 (or perfect pre-
 411 diction) line with little variability between each iteration. Once again, there is no skill
 412 in predicting the year of the observations for the ANN trained on the AER+ simulation.
 413 In ALL, the median slope is greater than the 1:1 line likely due to the fact that a forced
 414 temperature signal does not emerge until after the middle of the 20th century.

415 While the results in Figures 3 and 4 show predictions based on maps of annual mean
 416 2-m temperature, we also investigate differences by calculating seasonal means before
 417 training and testing the ANN. Figure S9 show the results of predicting the year for bo-
 418 real winter (January-February-March; JFM) and boreal summer (July-August-September;
 419 JAS) in the ANNs using GHG+ and ALL, respectively. Once more, we find that the cor-
 420 relation of the predicted year of observations is higher for the ANN trained on GHG+.
 421 Notably, we also find a higher correlation for observations in JAS relative to JFM for
 422 both GHG+ and ALL trained ANNs. This may be a result of greater internal variabil-
 423 ity of 2-m temperatures in the Northern Hemisphere during JFM. In other words, the
 424 indicator patterns in common between observations and the climate model data may be
 425 weaker in boreal winter compared to summer.

426 To understand how the ANN is making its predictions, we utilize LRP for evalu-
 427 ating regional climate patterns of interest. In particular, we investigate why the ANN
 428 predictions of observations are better correlated to the actual year after training on a
 429 climate simulation without time-evolving aerosols. As a reminder, the LRP heatmaps
 430 indicate areas of “relevance” (or importance) for the ANN to make an accurate predic-
 431 tion. Therefore, greater relevance does not necessarily correspond to the locations of great-
 432 est climate forcing. Additionally, the locations of higher relevance may change over time.

433 **3.2 Uncertainty in Layer-wise Relevance Propagation**

434 The LRP algorithm employed here provides output (relevance) for all grid points
 435 of every sample (e.g., Figure 1). However, it can be difficult to distinguish physically mean-
 436 ingful regions of importance to the ANN, especially for identifying known climate sig-
 437 nals. To limit noise in our LRP maps, we compute a threshold (or statistical significance)

438 using a baseline relevance value. In other words, we determine the maximum feature rel-
 439 evance that could be expected from an ANN that is trained on random noise. While other
 440 uncertainty metrics for LRP have been proposed (e.g., Bykov et al., 2020; Fabi & Schnei-
 441 der, 2020), our simple method can be employed without modifying the existing ANN ar-
 442 chitecture or LRP algorithm and takes a common approach applied by climate scientists.

443 We compute this baseline relevance threshold as follows: (1) we randomly shuffle
 444 the individual ensemble member and year dimensions of the ALL input data while keep-
 445 ing the true year fixed (not shuffling), (2) we proceed with training and testing using the
 446 same ANN architecture and hyperparameters as Section 2.3, (3) each output sample is
 447 then propagated backward into the ANN to compute the relevance map, (4) we repeat
 448 steps 1-3 for 500 iterations of the ANN by using unique random initialization seeds and
 449 taking different combinations of the training and testing data, and (5) finally, we com-
 450 pute the 95th percentile from the distribution of LRP values at all grid points that are
 451 obtained from this procedure. Thus, this bootstrapping-like method determines the dis-
 452 tribution of LRP values that could be expected from climate data with no serial auto-
 453 correlation or temporal trends from forced signals.

454 Figure 5 displays a histogram of this distribution of LRP values after 500 unique
 455 iterations of the shuffled ANN. We also test our observations (20CRv3) on the ANN trained
 456 by the shuffled ensemble from steps (1)-(5). As expected, the ANN cannot predict the
 457 year (median linear slope near 0), since it is unable to learn any forced climate signals
 458 from the shuffled data. Figure S10 shows a histogram of possible R^2 values from the lin-
 459 ear fit of observations compared to the median R^2 of observations trained on either AER+,
 460 GHG+, or ALL (Section 3.1.2). We also show an example of a LRP map from a single
 461 iteration of the ANN trained on the shuffled ensemble, which highlights the lack of rel-
 462 evant regions for the ANN to make a decision on this synthetic data (Figure 5).

463 As an additional check of our methodology, we create a “large ensemble” of ran-
 464 dom numbers drawn from a normal distribution. This large ensemble of random noise
 465 has the same dimensions as our real data (20 ensembles, 161 years, 96 by 144 spatial grid
 466 points). After repeating steps (2)-(5), we find that the 95th percentile of the random noise
 467 LRP is in close agreement with our baseline calculated from Figure 5 (not shown).

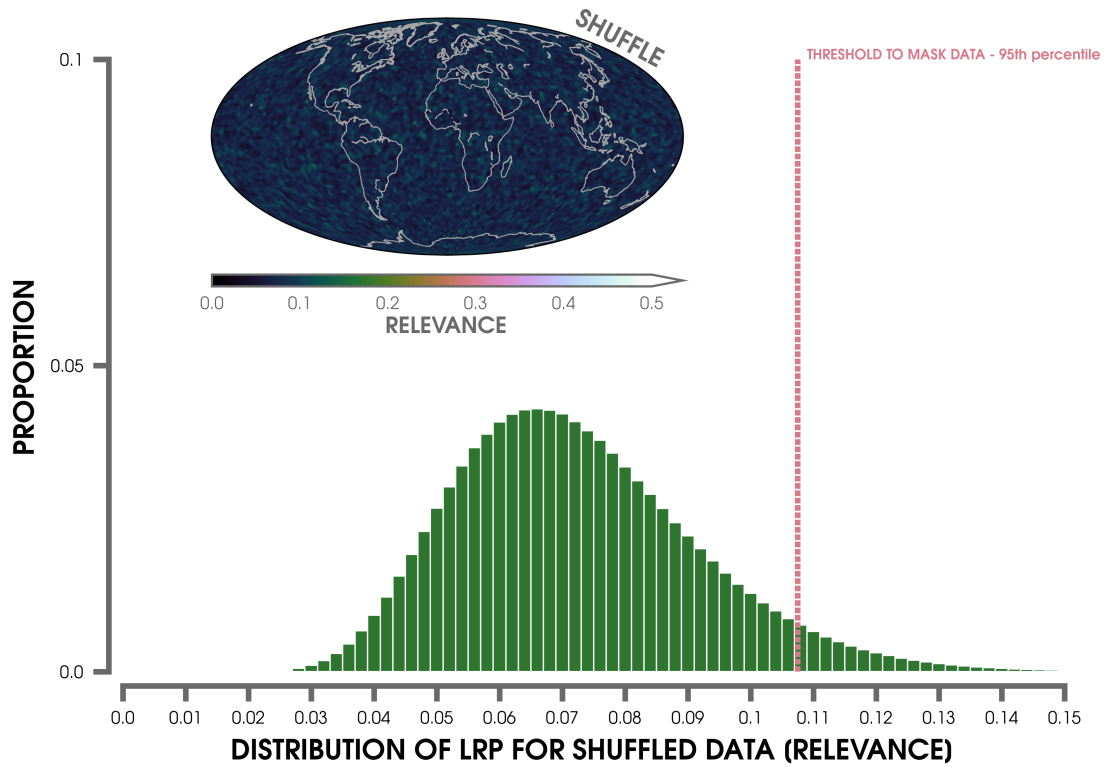


Figure 5. Histogram of the possible relevance values from LRP after randomly shuffling the ensemble members and years of the input data using the ALL experiment (see text for details). The 95th percentile LRP threshold is shown by the dashed vertical red line. The graph inset shows a LRP composite heatmap for one ANN trained on the shuffled input data and averaged across all years. Higher LRP values indicate greater relevance for the ANN’s prediction.

3.3 Regions of Climate Signal

Figure 6 show the LRP heatmaps for the individual ANN’s trained on AER+, GHG+, and ALL input data of annual mean 2-m temperature masked using the method outlined in Section 3.2. Our LRP maps are averaged for every prediction sample (ensemble member) that is accurate to within ± 2 years of the actual year (Barnes et al., 2020). In Figure 6, we show the temporal evolution of relevance for the four periods we have considered in this study (e.g., Figure 2). These LRP maps are composites after masking out the relevance below our new uncertainty threshold (see Figure 5). To compare the influence of our LRP uncertainty metric introduced in Section 3.2, we also show the same LRP heatmaps in Figure S11, but without using a mask. Comparing Figure 6 to Figure S11, we now see several climate regions of interest (e.g., North Atlantic and Southeast Asia) that are more clearly distinguishable from the background noise.

The North Atlantic is a key region of relevance between all three large ensembles, but is largest in GHG+ during the 2000 to 2039 period (Figure 6g). The LRP maps also reveal Southeast Asia as an important region for the AER+ and ALL neural networks. The relevance is largest in Southeast Asia for AER+ during the early 20th (Figure 6a) and early 21st centuries (Figure 6c). Again, although the regions of relevance do not directly correspond to surface forcing, we infer that the emissions of anthropogenic aerosols over Southeast Asia and India are important indicators for the ANN to predict the year in the AER+ and ALL large ensembles. We also find that the Southern Ocean is a significant region of relevance for the large ensembles that observe time-evolving greenhouse gases (GHG+ and ALL). Notably, this Southern Ocean signal appears along the Antarctic sea-ice edge. However, in agreement with Barnes et al. (2020), we find that the Arctic is not a region of importance for predicting the year in any of the large ensemble simulations. Despite the effects of Arctic amplification, the lack of relevance to the ANN prediction is likely a result of the large atmospheric internal variability in the high latitudes relative to the tropics (Figure S4).

To compare the differences in LRP maps between seasonal and annual mean input data, we show their relevance composites over 1960 to 2039 in Figure 7. This period is selected due to the greater differences in the ToE of forced signals between the three large ensembles (Section 3.1.1). For the LRP maps based on the annual mean data (Figures 7a,f,k), we observe higher relevance in the North Atlantic for AER+, GHG+,

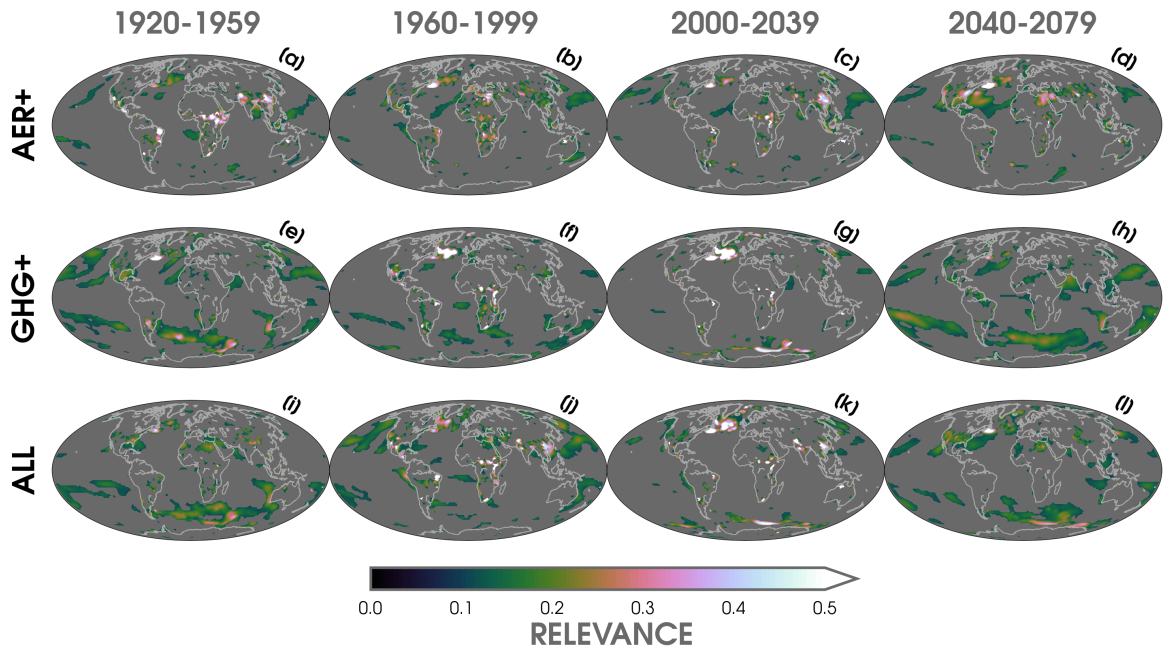


Figure 6. LRP composite heatmaps averaged over 1920 to 1959 (a,e,i), 1960 to 1999 (b,f,j), 2000 to 2039 (c,g,k), and 2040 to 2079 (d,h,l) for the three large ensemble experiments (AER+; a-d, GHG+; e-h, ALL; i-l). Higher LRP values indicate greater relevance for the ANN’s prediction. Relevance values less than the 95th percentile threshold (see text) have been masked out (gray shading).

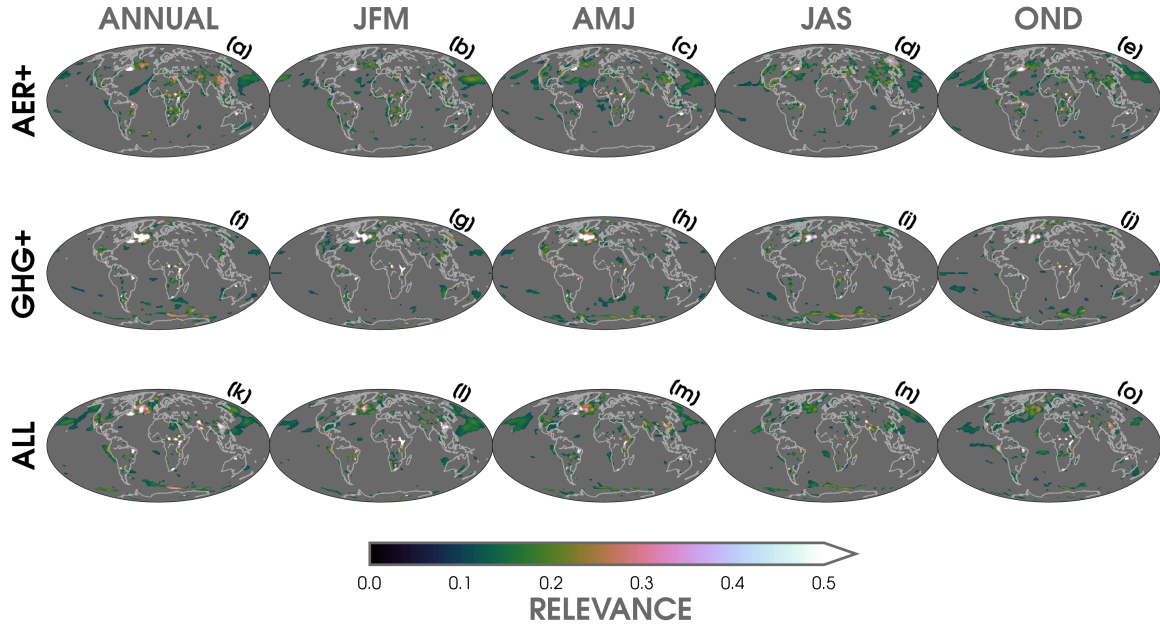


Figure 7. LRP heatmaps for ANNs trained separately on annual (a,f,k), January-March (JFM; b,g,l), April-June (AMJ; c,h,m), July-September (JAS; d,i,n), and October-December (OND; e,j,o) input data of 2-m temperature using the three large ensemble experiments (AER+; a-e, GHG+; f-j, ALL; k-o). Every LRP map is composited over the 1960 to 2039 period for the annual data and in each season. Higher LRP values indicate greater relevance for the ANN’s prediction. Relevance values less than the 95th percentile threshold (see text) have been masked out (gray shading).

500 and ALL neural networks. This area of relevance is largest in the ANN trained on GHG+
 501 and is somewhat consistent between seasons. In agreement with Figure 6, this shows that
 502 the North Atlantic is a particularly important region for the neural network to predict
 503 the year. For AER+ and ALL, we observe a relevance hotspot over India and Southeast
 504 Asia, which is distinct during JFM and OND. This is likely due to the local influence
 505 of time-evolving aerosols in these climate model simulations, which are absent in the ANN
 506 trained on GHG+. Although there are some regional and seasonal differences in Figure
 507 7, the primary climate indicators (“relevance hotspots”) remain similar. Thus, we focus
 508 on the annual mean input data for the rest of our analysis.

509 As previously discussed (e.g., in Figure 4), we test the robustness of our results by
 510 running 100 unique iterations of each large ensemble ANN for different combinations of
 511 training and testing data. Figure S12a-c shows a composite LRP heatmap that is av-
 512 eraged over all 100 possible iterations of the ANN from 1920 to 2080 compared to a com-
 513 posite of ANNs using a smaller L_2 regularization parameter and larger epoch parame-
 514 ter (Figure S12d-f). The conclusions remain the same. The regions of greatest relevance
 515 are consistent with Figure 6 and point to the North Atlantic and portions of Southeast
 516 Asia (only in AER+ and ALL) as essential to the ANN’s predictions. This highlights
 517 that the regional signals are robust, even after considering different combinations of in-
 518 dividual ensemble members and a smaller regularization parameter.

519 Figure 8 shows the distribution of relevances from the 100 unique ANN iterations
 520 for the mean relevance value (1960-2039) in five general regions (Southeast Asia, India,
 521 North Atlantic, Central Africa, and a portion of the Southern Ocean). The small vari-
 522 ance in all of the distributions further reinforces the importance of these areas as key cli-
 523 mate indicator patterns that are learned by our nonlinear ANN. We find weaker rele-
 524 vance over Southeast Asia (Figure 8a) and India (Figure 8b) for GHG+, which is likely
 525 a result of its industrial aerosols being held fixed to 1920 levels. Thus, the temperature
 526 signals in these regions (e.g., absence of local cooling due to aerosols) are not as impor-
 527 tant for the ANN prediction. In contrast, GHG+ observes the greatest relevance in the
 528 North Atlantic, while AER+ observes the smallest relevance in this same area (Figure
 529 8c). Interestingly, the North Atlantic distribution for ALL falls between AER+ and GHG+.
 530 The relevance signals across Central Africa (Figure 8d) and the Southern Ocean (Fig-
 531 ure 8e) are mostly consistent between large ensemble simulations. Nevertheless, we note
 532 that there is a slight tendency for the Southern Ocean to be more important for the ANN
 533 when there is a larger relative contribution from greenhouse gas forcing (GHG+ and ALL).
 534 These LRP results highlight the key importance of the North Atlantic and Southeast Asia
 535 for the ANNs to make their predictions. To further compare their spatial differences of
 536 relevance, Figure S14 shows the difference in LRP heatmap composites for AER+ mi-
 537 nus ALL and GHG+ minus ALL. The largest contrasts in LRP are highlighted across
 538 Southeast Asia, the subpolar Atlantic, and parts of Central Africa.

539 Finally, to understand where the ANN focuses its attention when making predic-
 540 tions on real world data, Figure 9 shows LRP maps for the observations that are input
 541 into the ANNs. Similar to the previous LRP maps of the climate model training and test-

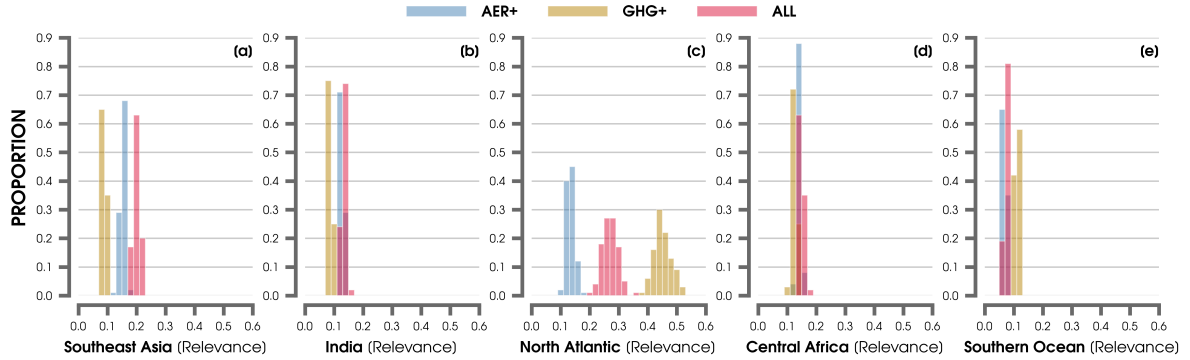


Figure 8. Histograms of mean relevance from LRP over Southeast Asia (a; 10-40°N and 105-120°E), India (b; 15-40°N and 70-105°E), the North Atlantic warming hole region (c; 50-60°N and 45-20°W), Central Africa (d; 0-15°N and 10°W-45°E), and a region near the Southern Ocean (e; 40-66°S and 5-70°E) for 100 unique iterations of the AER+ (blue), GHG+ (brown), and ALL (red) models. Mean LRP values are averaged over each year from 1960 to 2039.

542 ing data, we find several common relevance regions emerge (e.g., North Atlantic and South-
 543 east Asia). However, recall that the prediction of the years for observations are strikingly
 544 different between each large ensemble ANN (Figure 3). In particular, the GHG+ neu-
 545 ral network is more skillful in predicting the order of the years than by ALL. While there
 546 is somewhat greater relevance using observations across the North Atlantic and South-
 547 ern Ocean for the ANN trained on GHG+ (Figure 9c-9d) compared to ALL (Figure 9e-
 548 9f), the general patterns between the LRP maps are similar. This indicates that the neu-
 549 ral networks are using different combinations of these regional temperature signals to pre-
 550 dict the observations. This also suggests that the GHG+ network may be more skillful
 551 by focusing on greenhouse gas-induced responses that are closer to real world data, rather
 552 than the temperature patterns which are modulated by industrial aerosol forcing in the
 553 AER+ and ALL large ensembles. Hence, the LRP maps reveal how industrial aerosols
 554 can either mask or augment detection of greenhouse gas-induced warming signals on lo-
 555 cal to regional scales.

556 4 Discussion and Conclusions

557 Due to complex interactions between internal and external forcings in the climate
 558 system, it remains difficult to estimate the local and regional influence of human-induced

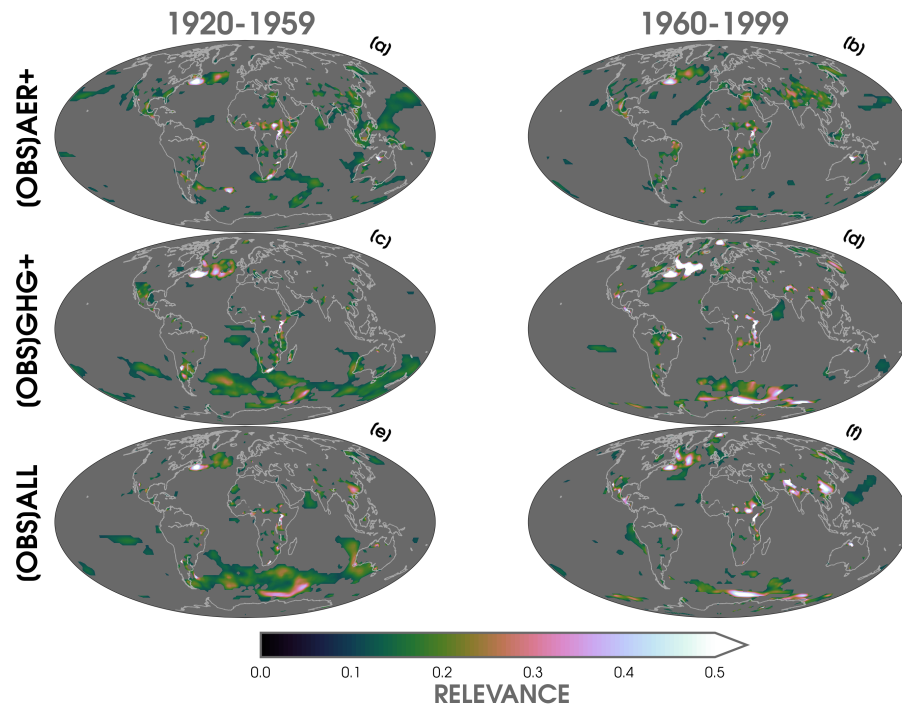


Figure 9. LRP composite heatmaps (annual mean) averaged over 1920 to 1959 (a,c,e) and 1960 to 1999 (b,d,f) for observations (OBS) tested separately on each large ensemble ANN (AER+; a-b, GHG+; c-d, ALL; e-f). Higher LRP values indicate greater relevance for the ANN’s prediction. Relevance values less than the 95th percentile threshold (see text) have been masked out (gray shading).

559 climate change on surface air temperatures (Schneider & Held, 2001; Deser et al., 2012;
560 McKinnon & Deser, 2018). Our work demonstrates the utility of explainable artificial
561 intelligence (XAI) methods for extracting patterns of climate signals due to varying ex-
562 ternal forcing, which adds to an existing set of statistical techniques for evaluating signal-
563 to-noise in the Earth system (e.g., Wills, Sippel, & Barnes, 2020). By leveraging a XAI
564 tool as a novel pattern recognition method, we aim to understand how a nonlinear ar-
565 tificial neural network (ANN) makes a prediction by learning regional climate signals.

566 We build off of ANN results from Barnes et al. (2019, 2020) by investigating the
567 role of different anthropogenic external forcings on temperature patterns relative to the
568 influence of atmospheric internal variability. Using climate model data from a new set
569 of large ensemble experiments, we compare different combinations of human-induced cli-
570 mate drivers (greenhouse gases and industrial aerosols) on forced temperature signals
571 over the 20th and 21st centuries. The large number of ensemble members from one fully-
572 coupled climate model (CESM1) allow us to disentangle forced changes from internal vari-
573 ability. In particular, we use layer-wise relevance propagation (LRP) to investigate how
574 the ANN learns regional climate patterns in order to predict the year from inputs of 2-
575 m air temperatures. Importantly, LRP allows us to investigate the time-evolving rele-
576 vance (from 1920 to 2080) of input features (maps of 2-m temperature) for the ANN to
577 make an accurate prediction. We also introduce a simple metric to further extract the
578 key relevance regions from the LRP maps. Lastly, we test our nonlinear ANN on obser-
579 vations from a new 20th century atmospheric reanalysis data set (20CRv3) in order to
580 understand how the effect of different external climate forcings impact the prediction of
581 our ANN after testing on real world data.

582 While efforts are underway to constrain observational uncertainties for the effec-
583 tive radiative forcing of aerosols (e.g., Yoshioka et al., 2019; Bellouin et al., 2020; Ben-
584 der, 2020; C. Smith et al., 2020), the net influence of aerosols on regional temperature
585 variability remains highly uncertain in historical and future climate model simulations
586 (Bauer et al., 2020; Dittus et al., 2020; Peace et al., 2020). Surprisingly, we found that
587 our ANN trained on a climate model simulation with fixed industrial aerosols (set to 1920
588 levels; GHG+) made predictions made predictions of real world temperature observa-
589 tions that correlated higher with the actual year. In contrast, the ANN trained on a large
590 ensemble with the most realistic external forcing configuration (ALL) was less likely to
591 correctly identify the order of the years for observations. The LRP maps based on ob-

592 observations indicate that the temperature signal in the North Atlantic is particularly rel-
 593 evant for the predictions by the ANN trained on GHG+ compared to ALL. We also note
 594 that the spatial features of the LRP maps are similar to areas of anomalously late or early
 595 temperature signals in the ToE maps (relative to the rest of the globe), especially across
 596 Southeast Asia, Central Africa, and the North Atlantic. Explainable AI tools, such as
 597 LRP, may be another promising tool to explore for identifying the emergence of other
 598 climate variables in future work.

599 Our ANN results suggests that CESM1 is highly sensitive to combinations between
 600 external forcings when simulating the variability and timing of emergence of global cli-
 601 mate signals, such as the North Atlantic Warming Hole, compared to observations. While
 602 we focus on only one set of single-forcing large ensembles, we recommend that additional
 603 experiments are conducted to fully understand the sensitivity of GCMs to aerosol radia-
 604 tive forcing and subsequently simulate realistic temperature trends and variability.

605 **Acknowledgments**

606 We thank two anonymous reviewers and the Editor for their constructive suggestions,
 607 which substantially improved our study. This work was supported by NOAA MAPP grant
 608 NA19OAR4310289. We would also like to acknowledge the CESM Large Ensemble Com-
 609 munity Project and CISL supercomputing resources provided by NCAR ([doi:10.5065/
 610 D6RX99HX](https://doi.org/10.5065/D6RX99HX)). Support for the 20CRv3 dataset is provided by the U.S. Department of En-
 611 ergy (DOE) Office of Science Biological and Environmental Research (BER), by the NOAA
 612 CPO, and by the NOAA PSL.

613 **Data Availability Statements**

614 The CESM1 Large Ensemble simulations used in this study are freely available ([https://
 615 www.cesm.ucar.edu/projects/community-projects/LENS/data-sets.html](https://www.cesm.ucar.edu/projects/community-projects/LENS/data-sets.html)). Monthly
 616 20th Century Reanalysis V3 (20CRv3) data are provided by the NOAA/OAR/ESRL PSL,
 617 Boulder, Colorado, USA, from their website at <https://psl.noaa.gov/>. Monthly re-
 618 analysis data for ERA5 are also freely available available ([https://climate.copernicus
 619 .eu/climate-reanalysis](https://climate.copernicus.eu/climate-reanalysis)). Computer code for the ANN architecture and exploratory
 620 data analysis is available at <https://zenodo.org/record/4665793>. Figures and anal-
 621 ysis were completed using Python v3.7.6, Numpy v1.19 (Harris et al., 2020), SciPy v1.4.1
 622 (Virtanen et al., 2020), Matplotlib v3.2.2 (Hunter, 2007), and colormaps provided by cmo-

623 cean v2.0 (Thyng et al., 2016) and Scientific v7.0.0 (Crameri, 2018; Crameri et al., 2020).
 624 Additional Python packages used for development of the ANN and LRP visualizations
 625 include Keras/TensorFlow (Abadi et al., 2016) and iNNvestigate (Alber et al., 2019). Ref-
 626 erences for the data sets are provided throughout the study.

627 **References**

- 628 Abadi, M., Barham, P., Chen, J., Chen, Z., Davis, A., Dean, J., . . . Zheng, X.
 629 (2016). TensorFlow: A system for large-scale machine learning. In *Proceedings*
 630 *of the 12th usenix symposium on operating systems design and implementation,*
 631 *osdi 2016.*
- 632 Agarap, A. F. (2018, mar). Deep Learning using Rectified Linear Units (ReLU).
 633 *arXiv*. Retrieved from <http://arxiv.org/abs/1803.08375>
- 634 Alber, M., Lapuschkin, S., Seegerer, P., Hägele, M., Schütt, K. T., Montavon, G., . . .
 635 Kindermans, P. J. (2019). iNNvestigate neural networks! *Journal of Machine*
 636 *Learning Research, 20.*
- 637 Allen, R. J., & Sherwood, S. C. (2011, may). The impact of natural versus an-
 638 thropogenic aerosols on atmospheric circulation in the Community Atmo-
 639 sphere Model. *Climate Dynamics, 36*(9-10), 1959–1978. Retrieved from
 640 <https://link.springer.com/article/10.1007/s00382-010-0898-8> doi:
 641 10.1007/s00382-010-0898-8
- 642 Amo, A., Montero, J., Biging, G., & Cutello, V. (2004, jul). Fuzzy classification sys-
 643 tems. *European Journal of Operational Research, 156*(2), 495–507. doi: 10
 644 .1016/S0377-2217(03)00002-X
- 645 Bach, S., Binder, A., Montavon, G., Klauschen, F., Müller, K. R., & Samek, W.
 646 (2015, jul). On pixel-wise explanations for non-linear classifier decisions by
 647 layer-wise relevance propagation. *PLoS ONE, 10*(7), e0130140. Retrieved from
 648 <http://www.hfsp.org/>, doi: 10.1371/journal.pone.0130140
- 649 Barnes, E. A., Hurrell, J. W., Ebert-Uphoff, I., Anderson, C., & Anderson, D. (2019,
 650 nov). Viewing Forced Climate Patterns Through an AI Lens. *Geophysical Re-*
 651 *search Letters, 46*(22), 13389–13398. Retrieved from <https://onlinelibrary>
 652 [.wiley.com/doi/abs/10.1029/2019GL084944](https://onlinelibrary.wiley.com/doi/abs/10.1029/2019GL084944) doi: 10.1029/2019GL084944
- 653 Barnes, E. A., Toms, B., Hurrell, J. W., Ebert-Uphoff, I., Anderson, C., & Ander-
 654 son, D. (2020, sep). Indicator Patterns of Forced Change Learned by an

- 655 Artificial Neural Network. *Journal of Advances in Modeling Earth Systems*,
656 12(9). Retrieved from [https://onlinelibrary.wiley.com/doi/10.1029/](https://onlinelibrary.wiley.com/doi/10.1029/2020MS002195)
657 2020MS002195 doi: 10.1029/2020MS002195
- 658 Bauer, S. E., Tsigaridis, K., Faluvegi, G., Kelley, M., Lo, K. K., Miller, R. L., ...
659 Wu, J. (2020, aug). Historical (1850–2014) Aerosol Evolution and Role on
660 Climate Forcing Using the GISS ModelE2.1 Contribution to CMIP6. *Journal*
661 *of Advances in Modeling Earth Systems*, 12(8). Retrieved from [https://](https://agupubs.onlinelibrary.wiley.com/doi/full/10.1029/2019MS001978)
662 agupubs.onlinelibrary.wiley.com/doi/full/10.1029/2019MS001978 doi:
663 10.1029/2019MS001978
- 664 Bellouin, N., Quaas, J., Gryspeerdt, E., Kinne, S., Stier, P., Watson-Parris, D., ...
665 Stevens, B. (2020, mar). *Bounding Global Aerosol Radiative Forcing of Climate*
666 *Change* (Vol. 58) (No. 1). Blackwell Publishing Ltd. Retrieved from [https://](https://agupubs.onlinelibrary.wiley.com/doi/full/10.1029/2019RG000660)
667 agupubs.onlinelibrary.wiley.com/doi/full/10.1029/2019RG000660 doi:
668 10.1029/2019RG000660
- 669 Bender, F. A. (2020). Aerosol Forcing: Still Uncertain, Still Relevant. *AGU Ad-*
670 *vances*, 1(3). doi: 10.1029/2019av000128
- 671 Beucler, T., Rasp, S., Pritchard, M., & Gentine, P. (2019, jun). Achieving Conserva-
672 tion of Energy in Neural Network Emulators for Climate Modeling. *arXiv*. Re-
673 trieved from <http://arxiv.org/abs/1906.06622>
- 674 Bevan, J. M., & Kendall, M. G. (1971). Rank Correlation Methods. *The Statisti-*
675 *cian*. doi: 10.2307/2986801
- 676 Bonfils, C. J., Santer, B. D., Fyfe, J. C., Marvel, K., Phillips, T. J., & Zimmer-
677 man, S. R. (2020). Human influence on joint changes in temperature,
678 rainfall and continental aridity. *Nature Climate Change*, 10(8). doi:
679 10.1038/s41558-020-0821-1
- 680 Booth, B. B., Harris, G. R., Jones, A., Wilcox, L., Hawcroft, M., & Carslaw, K. S.
681 (2018). *Comments on "Rethinking the lower bound on aerosol radiative forc-*
682 *ing"* (Vol. 31) (No. 22). doi: 10.1175/JCLI-D-17-0369.1
- 683 Botari, T., Hvilshøj, F., Izbicki, R., & de Carvalho, A. C. P. L. F. (2020, sep). Me-
684 LIME: Meaningful Local Explanation for Machine Learning Models. *arXiv*.
685 Retrieved from <http://arxiv.org/abs/2009.05818>
- 686 Boukabara, S.-A., Krasnopolsky, V., Penny, S. G., Stewart, J. Q., & McGovern,
687 A. (2020). Outlook for Exploiting Artificial Intelligence in the Earth

- 688 and Environmental Sciences *. *Bulletin of the American Meteorologi-*
689 *cal Society*, 1–53. Retrieved from [http://journals.ametsoc.org/bams/](http://journals.ametsoc.org/bams/article-pdf/doi/10.1175/BAMS-D-20-0031.1/5018772/bamsd200031.pdf)
690 [article-pdf/doi/10.1175/BAMS-D-20-0031.1/5018772/bamsd200031.pdf](http://journals.ametsoc.org/bams/article-pdf/doi/10.1175/BAMS-D-20-0031.1/5018772/bamsd200031.pdf)
691 doi: 10.1175/BAMS-D-20-0031.1
- 692 Bykov, K., Höhne, M. M. C., Müller, K.-R., Nakajima, S., & Kloft, M. (2020, jun).
693 How Much Can I Trust You? – Quantifying Uncertainties in Explaining Neural
694 Networks. *arXiv*. Retrieved from <http://arxiv.org/abs/2006.09000>
- 695 Chemke, R., Zanna, L., & Polvani, L. M. (2020). Identifying a human signal in the
696 North Atlantic warming hole. *Nature Communications*, 11(1). doi: 10.1038/
697 s41467-020-15285-x
- 698 Compo, G. P., Whitaker, J. S., Sardeshmukh, P. D., Matsui, N., Allan, R. J.,
699 Yin, X., ... Worley, S. J. (2011, jan). *The Twentieth Century Reanalysis*
700 *Project* (Vol. 137) (No. 654). John Wiley and Sons Ltd. Retrieved from
701 <https://rmets.onlinelibrary.wiley.com/doi/full/10.1002/qj.776> doi:
702 10.1002/qj.776
- 703 Crameri, F. (2018, jan). Scientific colour maps. *Zenodo*. Retrieved from [https://](https://zenodo.org/record/4153113)
704 zenodo.org/record/4153113 doi: 10.5281/ZENODO.4153113
- 705 Crameri, F., Shephard, G. E., & Heron, P. J. (2020, dec). The misuse of colour
706 in science communication. *Nature Communications*, 11(1), 1–10. Retrieved
707 from <https://doi.org/10.1038/s41467-020-19160-7> doi: 10.1038/s41467-
708 -020-19160-7
- 709 Dagan, G., Stier, P., & Watson-Parris, D. (2020, nov). Aerosol forcing masks
710 and delays the formation of the North-Atlantic warming hole by three
711 decades. *Geophysical Research Letters*, 47(22). Retrieved from [https://](https://agupubs.onlinelibrary.wiley.com/doi/full/10.1029/2020GL090778)
712 agupubs.onlinelibrary.wiley.com/doi/full/10.1029/2020GL090778 doi:
713 10.1029/2020gl090778
- 714 Deng, J., Dai, A., & Xu, H. (2020, jan). Nonlinear climate responses to increas-
715 ing CO2 and anthropogenic aerosols simulated by CESM1. *Journal of Climate*,
716 33(1), 281–301. Retrieved from www.ametsoc.org/PUBSReuseLicenses doi:
717 10.1175/JCLI-D-19-0195.1
- 718 Deser, C. (2020, nov). Certain uncertainty: The role of internal climate variabil-
719 ity in projections of regional climate change and risk management. *Earth's*
720 *Future*. Retrieved from <https://onlinelibrary.wiley.com/doi/10.1029/>

- 721 2020EF001854 doi: 10.1029/2020EF001854
- 722 Deser, C., Lehner, F., Rodgers, K. B., Ault, T., Delworth, T. L., DiNezio, P. N.,
 723 ... Ting, M. (2020, mar). Insights from Earth system model initial-condition
 724 large ensembles and future prospects. *Nature Climate Change*, 1–10. Re-
 725 trieved from <http://www.nature.com/articles/s41558-020-0731-2> doi:
 726 10.1038/s41558-020-0731-2
- 727 Deser, C., Phillips, A., Bourdette, V., & Teng, H. (2012, feb). Uncertainty in climate
 728 change projections: the role of internal variability. *Climate Dynamics*, 38(3-4),
 729 527–546. Retrieved from [http://link.springer.com/10.1007/s00382-010-](http://link.springer.com/10.1007/s00382-010-0977-x)
 730 [0977-x](http://link.springer.com/10.1007/s00382-010-0977-x) doi: 10.1007/s00382-010-0977-x
- 731 Deser, C., Phillips, A. S., Simpson, I. R., Rosenbloom, N., Coleman, D., Lehner, F.,
 732 ... Stevenson, S. (2020, sep). Isolating the Evolving Contributions of An-
 733 thropogenic Aerosols and Greenhouse Gases: A New CESM1 Large Ensemble
 734 Community Resource. *Journal of Climate*, 33(18), 7835–7858. Retrieved from
 735 <https://doi.org/10.1175/JCLI-D-20-> doi: 10.1175/JCLI-D-20
- 736 Deser, C., Terray, L., & Phillips, A. S. (2016). Forced and internal compo-
 737 nents of winter air temperature trends over North America during the past
 738 50 years: Mechanisms and implications. *Journal of Climate*, 29(6). doi:
 739 10.1175/JCLI-D-15-0304.1
- 740 Dittus, A. J., Hawkins, E., Wilcox, L. J., Sutton, R. T., Smith, C. J., Andrews,
 741 M. B., & Forster, P. M. (2020, jul). Sensitivity of Historical Climate
 742 Simulations to Uncertain Aerosol Forcing. *Geophysical Research Letters*,
 743 47(13). Retrieved from [https://onlinelibrary.wiley.com/doi/10.1029/](https://onlinelibrary.wiley.com/doi/10.1029/2019GL085806)
 744 [2019GL085806](https://onlinelibrary.wiley.com/doi/10.1029/2019GL085806) doi: 10.1029/2019GL085806
- 745 Ebert-Uphoff, I., Samarasinghe, S., & Barnes, E. (2019). Thoughtfully Using Artifi-
 746 cial Intelligence in Earth Science. *Eos*, 100. doi: 10.1029/2019eo135235
- 747 Fabi, K., & Schneider, J. (2020, aug). On Feature Relevance Uncertainty: A Monte
 748 Carlo Dropout Sampling Approach. *arXiv*. Retrieved from [http://arxiv](http://arxiv.org/abs/2008.01468)
 749 [.org/abs/2008.01468](http://arxiv.org/abs/2008.01468)<http://dx.doi.org/10.5281/zenodo.3970396> doi: 10
 750 [.5281/zenodo.3970396](http://dx.doi.org/10.5281/zenodo.3970396)
- 751 Flynn, C. M., & Mauritsen, T. (2020). On the climate sensitivity and historical
 752 warming evolution in recent coupled model ensembles. *Atmospheric Chemistry*
 753 *and Physics*, 20(13). doi: 10.5194/acp-20-7829-2020

- 754 Friedman, J. H. (2012, jul). Fast sparse regression and classification. *International*
 755 *Journal of Forecasting*, 28(3), 722–738. doi: 10.1016/j.ijforecast.2012.05.001
- 756 Gagne, D. J., Haupt, S. E., Nychka, D. W., & Thompson, G. (2019, aug). *In-*
 757 *terpretable deep learning for spatial analysis of severe hailstorms* (Vol. 147)
 758 (No. 8). American Meteorological Society. doi: 10.1175/MWR-D-18-0316.1
- 759 Giese, B. S., Seidel, H. F., Compo, G. P., & Sardeshmukh, P. D. (2016, sep).
 760 An ensemble of ocean reanalyses for 1815-2013 with sparse observational
 761 input. *Journal of Geophysical Research: Oceans*, 121(9), 6891–6910.
 762 Retrieved from <http://doi.wiley.com/10.1002/2016JC012079> doi:
 763 10.1002/2016JC012079
- 764 Goodfellow, I., Bengio, Y., & Courville, A. (2016). *Deep Learning*.
- 765 Harris, C. R., Jarrod Millman, K., van der Walt, S. J., Gommers, R., Virtanen, P.,
 766 Cournapeau, D., ... Oliphant, T. E. (2020, sep). Array programming with
 767 NumPy. *Nature*, 585(7825), 357. Retrieved from [https://doi.org/10.1038/](https://doi.org/10.1038/s41586-020-2649-2)
 768 [s41586-020-2649-2](https://doi.org/10.1038/s41586-020-2649-2) doi: 10.1038/s41586-020-2649-2
- 769 Haustein, K., Otto, F. E., Venema, V., Jacobs, P., Cowtan, K., Hausfather, Z.,
 770 ... Schurer, A. P. (2019). A limited role for unforced internal vari-
 771 ability in twentieth-century warming. *Journal of Climate*, 32(16). doi:
 772 10.1175/JCLI-D-18-0555.1
- 773 Hawkins, E., Ortega, P., Suckling, E., Schurer, A., Hegerl, G., Jones, P., ... Van
 774 Oldenborgh, G. J. (2017, sep). Estimating changes in global temperature
 775 since the preindustrial period. *Bulletin of the American Meteorological So-*
 776 *ciety*, 98(9), 1841–1856. Retrieved from [http://journals.ametsoc.org/](http://journals.ametsoc.org/bams/article-pdf/98/9/1841/3747963/bams-d-16-0007{_}1.pdf)
 777 [bams/article-pdf/98/9/1841/3747963/bams-d-16-0007{_}1.pdf](http://journals.ametsoc.org/bams/article-pdf/98/9/1841/3747963/bams-d-16-0007{_}1.pdf) doi:
 778 10.1175/BAMS-D-16-0007.1
- 779 Hawkins, E., & Sutton, R. (2009, aug). The Potential to Narrow Uncertainty in
 780 Regional Climate Predictions. *Bulletin of the American Meteorological Society*,
 781 90(8), 1095–1107. doi: 10.1175/2009BAMS2607.1
- 782 Hawkins, E., & Sutton, R. (2016, jun). Connecting climate model projections
 783 of global temperature change with the real world. *Bulletin of the Amer-*
 784 *ican Meteorological Society*, 97(6), 963–980. Retrieved from [https://](https://journals.ametsoc.org/view/journals/bams/97/6/bams-d-14-00154.1.xml)
 785 journals.ametsoc.org/view/journals/bams/97/6/bams-d-14-00154.1.xml
 786 doi: 10.1175/BAMS-D-14-00154.1

- 787 Hegerl, G. C., Von Storch, H., Hasselmann, K., Santer, B. D., Cubasch, U., &
788 Jones, P. D. (1996). Detecting greenhouse-gas-induced climate change
789 with an optimal fingerprint method. *Journal of Climate*, 9(10). doi:
790 10.1175/1520-0442(1996)009<2281:DGGICC>2.0.CO;2
- 791 Hersbach, H., Bell, B., Berrisford, P., Hirahara, S., Horányi, A., Muñoz-Sabater,
792 J., ... Thépaut, J.-N. (2020, may). The ERA5 Global Reanalysis.
793 *Quarterly Journal of the Royal Meteorological Society*. Retrieved from
794 <https://onlinelibrary.wiley.com/doi/abs/10.1002/qj.3803> doi:
795 10.1002/qj.3803
- 796 Hunter, J. D. (2007, may). Matplotlib: A 2D graphics environment. *Computing in*
797 *Science and Engineering*, 9(3), 99–104. doi: 10.1109/MCSE.2007.55
- 798 Hurrell, J. W., Holland, M. M., Gent, P. R., Ghan, S., Kay, J. E., Kushner, P. J.,
799 ... Marshall, S. (2013). The community earth system model: A framework for
800 collaborative research. *Bulletin of the American Meteorological Society*, 94(9).
801 doi: 10.1175/BAMS-D-12-00121.1
- 802 Kadow, C., Hall, D. M., & Ulbrich, U. (2020, jun). Artificial intelligence reconstructs
803 missing climate information. *Nature Geoscience*, 1–6. doi: 10.1038/s41561-020-
804 -0582-5
- 805 Kay, J. E., Deser, C., Phillips, A., Mai, A., Hannay, C., Strand, G., ... Verten-
806 stein, M. (2015, aug). The Community Earth System Model (CESM)
807 Large Ensemble Project: A Community Resource for Studying Climate
808 Change in the Presence of Internal Climate Variability. *Bulletin of the*
809 *American Meteorological Society*, 96(8), 1333–1349. Retrieved from
810 <http://journals.ametsoc.org/doi/10.1175/BAMS-D-13-00255.1> doi:
811 10.1175/BAMS-D-13-00255.1
- 812 Keil, P., Mauritsen, T., Jungclaus, J., Hedemann, C., Olonscheck, D., & Ghosh, R.
813 (2020). Multiple drivers of the North Atlantic warming hole. *Nature Climate*
814 *Change*, 10(7). doi: 10.1038/s41558-020-0819-8
- 815 Knutti, R., Furrer, R., Tebaldi, C., Cermak, J., & Meehl, G. A. (2010). Challenges
816 in combining projections from multiple climate models. *Journal of Climate*,
817 23(10). doi: 10.1175/2009JCLI3361.1
- 818 Knutti, R., & Sedlacek, J. (2013, apr). Robustness and uncertainties in the new
819 CMIP5 climate model projections. *Nature Clim. Change*, 3(4), 369–373. doi:

- 820 10.1038/nclimate1716
- 821 Lagerquist, R., McGovern, A., Homeyer, C. R., Gagne, D. J., & Smith, T. (2020,
822 jul). Deep learning on three-dimensional multiscale data for next-hour
823 tornado prediction. *Monthly Weather Review*, *148*(7), 2837–2861. doi:
824 10.1175/MWR-D-19-0372.1
- 825 Lecun, Y., Bengio, Y., & Hinton, G. (2015, may). *Deep learning* (Vol. 521) (No.
826 7553). Nature Publishing Group. Retrieved from [https://www.nature.com/
827 articles/nature14539](https://www.nature.com/articles/nature14539) doi: 10.1038/nature14539
- 828 Lehner, F., Deser, C., Maher, N., Marotzke, J., Fischer, E., Brunner, L., ...
829 Hawkins, E. (2020). Partitioning climate projection uncertainty with mul-
830 tiple Large Ensembles and CMIP5/6. *Earth System Dynamics Discussions*,
831 1–28. doi: 10.5194/esd-2019-93
- 832 Lehner, F., Deser, C., & Terray, L. (2017). Toward a new estimate of "time of
833 emergence" of anthropogenic warming: Insights from dynamical adjustment
834 and a large initial-condition model ensemble. *Journal of Climate*, *30*(19). doi:
835 10.1175/JCLI-D-16-0792.1
- 836 Luysaert, S., Jammet, M., Stoy, P. C., Estel, S., Pongratz, J., Ceschia, E., ...
837 Dolman, A. J. (2014, apr). Land management and land-cover change have
838 impacts of similar magnitude on surface temperature. *Nature Climate Change*,
839 *4*(5), 389–393. Retrieved from www.nature.com/natureclimatechange doi:
840 10.1038/nclimate2196
- 841 Maher, N., Gupta, A. S., & England, M. H. (2014). *Drivers of decadal hiatus*
842 *periods in the 20th and 21st centuries* (Vol. 41) (No. 16). doi: 10.1002/
843 2014GL060527
- 844 Maher, N., Lehner, F., & Marotzke, J. (2020, may). Quantifying the role of internal
845 variability in the temperature we expect to observe in the coming decades.
846 *Environmental Research Letters*, *15*(5), 054014. Retrieved from [https://
847 doi.org/10.1088/1748-9326/ab7d02](https://doi.org/10.1088/1748-9326/ab7d02) doi: 10.1088/1748-9326/ab7d02
- 848 Maher, N., Milinski, S., Suarez-Gutierrez, L., Botzet, M., Dobrynin, M., Kornblueh,
849 L., ... Marotzke, J. (2019, jul). The Max Planck Institute Grand Ensemble:
850 Enabling the Exploration of Climate System Variability. *Journal of Advances*
851 *in Modeling Earth Systems*, *11*(7), 2050–2069. Retrieved from [https://
852 agupubs.onlinelibrary.wiley.com/doi/full/10.1029/2019MS001639](https://agupubs.onlinelibrary.wiley.com/doi/full/10.1029/2019MS001639) doi:

- 853 10.1029/2019MS001639
- 854 Mahlstein, I., Hegerl, G., & Solomon, S. (2012). Emerging local warming signals
855 in observational data. *Geophysical Research Letters*, *39*(21). doi: 10.1029/
856 2012GL053952
- 857 Mankin, J. S., Lehner, F., Coats, S., & McKinnon, K. A. (2020, oct). The Value
858 of Initial Condition Large Ensembles to Robust Adaptation Decision-Making.
859 *Earth's Future*, *8*(10). Retrieved from [https://onlinelibrary.wiley.com/](https://onlinelibrary.wiley.com/doi/10.1029/2020EF001610)
860 [doi/10.1029/2020EF001610](https://onlinelibrary.wiley.com/doi/10.1029/2020EF001610) doi: 10.1029/2020EF001610
- 861 Mann, H. B. (1945). Nonparametric Tests Against Trend. *Econometrica*. doi: 10
862 .2307/1907187
- 863 Mansfield, L. A., Nowack, P. J., Kasoar, M., Everitt, R. G., Collins, W. J., & Voul-
864 garakis, A. (2020). Predicting global patterns of long-term climate change from
865 short-term simulations using machine learning. *npj Climate and Atmospheric*
866 *Science*. Retrieved from <https://doi.org/10.1038/s41612-020-00148-5>
867 doi: 10.1038/s41612-020-00148-5
- 868 Marvel, K., Cook, B. I., Bonfils, C. J., Durack, P. J., Smerdon, J. E., & Williams,
869 A. P. (2019). Twentieth-century hydroclimate changes consistent with human
870 influence. *Nature*, *569*(7754). doi: 10.1038/s41586-019-1149-8
- 871 McGovern, A., Lagerquist, R., Gagne, D. J., Jergensen, G. E., Elmore, K. L., Home-
872 yer, C. R., & Smith, T. (2019, nov). Making the black box more transparent:
873 Understanding the physical implications of machine learning. *Bulletin of*
874 *the American Meteorological Society*, *100*(11), 2175–2199. Retrieved from
875 [http://journals.ametsoc.org/bams/article-pdf/100/11/2175/4876688/](http://journals.ametsoc.org/bams/article-pdf/100/11/2175/4876688/bams-d-18-0195-v1.pdf)
876 [bams-d-18-0195-v1.pdf](http://journals.ametsoc.org/bams/article-pdf/100/11/2175/4876688/bams-d-18-0195-v1.pdf) doi: 10.1175/BAMS-D-18-0195.1
- 877 McKinnon, K. A., & Deser, C. (2018). Internal variability and regional climate
878 trends in an observational large ensemble. *Journal of Climate*, *31*(17). doi: 10
879 .1175/JCLI-D-17-0901.1
- 880 Medhaug, I., Stolpe, M. B., Fischer, E. M., & Knutti, R. (2017). *Reconciling contro-*
881 *versies about the 'global warming hiatus'* (Vol. 545) (No. 7652). doi: 10.1038/
882 nature22315
- 883 Meehl, G. A., Hu, A., Castruccio, F., England, M. H., Bates, S. C., Danabasoglu,
884 G., ... Rosenbloom, N. (2020). Atlantic and Pacific tropics connected
885 by mutually interactive decadal-timescale processes. *Nature Geoscience*.

- 886 Retrieved from <https://doi.org/10.1038/s41561-020-00669-x> doi:
887 10.1038/s41561-020-00669-x
- 888 Meehl, G. A., Senior, C. A., Eyring, V., Flato, G., Lamarque, J. F., Stouffer, R. J.,
889 ... Schlund, M. (2020). *Context for interpreting equilibrium climate sensitivity*
890 *and transient climate response from the CMIP6 Earth system models* (Vol. 6)
891 (No. 26). doi: 10.1126/sciadv.aba1981
- 892 Menary, M. B., Robson, J., Allan, R. P., Booth, B. B., Cassou, C., Gastineau,
893 G., ... Zhang, R. (2020). Aerosol-Forced AMOC Changes in CMIP6
894 Historical Simulations. *Geophysical Research Letters*, 47(14). doi:
895 10.1029/2020GL088166
- 896 Milinski, S., Maher, N., & Olonscheck, D. (2020, oct). How large does a large en-
897 semble need to be? *Earth System Dynamics*, 11(4), 885–901. Retrieved from
898 <https://esd.copernicus.org/articles/11/885/2020/> doi: 10.5194/esd-11
899 -885-2020
- 900 Mitchell, D. M., Eunice Lo, Y. T., Seviour, W. J., Haimberger, L., & Polvani, L. M.
901 (2020, oct). The vertical profile of recent tropical temperature trends: Persis-
902 tent model biases in the context of internal variability. *Environmental Research*
903 *Letters*, 15(10). doi: 10.1088/1748-9326/ab9af7
- 904 Montavon, G., Lapuschkin, S., Binder, A., Samek, W., & Müller, K. R. (2017, may).
905 Explaining nonlinear classification decisions with deep Taylor decomposition.
906 *Pattern Recognition*, 65, 211–222. doi: 10.1016/j.patcog.2016.11.008
- 907 Montavon, G., Samek, W., & Müller, K. R. (2018, feb). *Methods for interpreting and*
908 *understanding deep neural networks* (Vol. 73). Elsevier Inc. doi: 10.1016/j.dsp
909 .2017.10.011
- 910 Neale, R. B., Gettelman, A., Park, S., Chen, C.-c., Lauritzen, P. H., Williamson,
911 D. L., ... Taylor, M. a. (2012). Description of the NCAR Community Atmo-
912 sphere Model (CAM 5.0). NCAR Technical Notes. *Ncar/Tn-464+Str*.
- 913 Oudar, T., Kushner, P. J., Fyfe, J. C., & Sigmond, M. (2018, sep). No Impact of
914 Anthropogenic Aerosols on Early 21st Century Global Temperature Trends
915 in a Large Initial-Condition Ensemble. *Geophysical Research Letters*, 45(17),
916 9245–9252. Retrieved from <http://doi.wiley.com/10.1029/2018GL078841>
917 doi: 10.1029/2018GL078841
- 918 Peace, A. H., Carslaw, K. S., Lee, L. A., Regayre, L. A., Booth, B. B., Johnson,

- 919 J. S., & Bernie, D. (2020). Effect of aerosol radiative forcing uncertainty on
920 projected exceedance year of a 1.5 °c global temperature rise. *Environmental*
921 *Research Letters*, 15(9). doi: 10.1088/1748-9326/aba20c
- 922 Peters, G. P., & Hausfather, Z. (2020). Emissions - the 'business as usual' story is
923 misleading. *Nature*, 577.
- 924 Polvani, L. M., Waugh, D. W., Correa, G. J., & Son, S. W. (2011, feb). Strato-
925 spheric ozone depletion: The main driver of twentieth-century atmospheric
926 circulation changes in the Southern Hemisphere. *Journal of Climate*, 24(3),
927 795–812. Retrieved from [http://journals.ametsoc.org/jcli/article-pdf/
928 24/3/795/3979461/2010jcli3772{_}1.pdf](http://journals.ametsoc.org/jcli/article-pdf/24/3/795/3979461/2010jcli3772{_}1.pdf) doi: 10.1175/2010JCLI3772.1
- 929 Qin, M., Dai, A., & Hua, W. (2020, oct). Quantifying contributions of internal
930 variability and external forcing to Atlantic multidecadal variability since
931 1870. *Geophysical Research Letters*, 47(22). Retrieved from [https://
932 agupubs.onlinelibrary.wiley.com/doi/full/10.1029/2020GL089504](https://agupubs.onlinelibrary.wiley.com/doi/full/10.1029/2020GL089504)
933 doi: 10.1029/2020gl089504
- 934 Rasp, S., Dueben, P. D., Scher, S., Weyn, J. A., Mouatadid, S., & Thuerey, N.
935 (2020, feb). *Weatherbench: A benchmark dataset for data-driven weather fore-
936 casting* (Vol. 12) (No. 11). American Geophysical Union (AGU). Retrieved
937 from [https://agupubs.onlinelibrary.wiley.com/doi/full/10.1029/
938 2020MS002203](https://agupubs.onlinelibrary.wiley.com/doi/full/10.1029/2020MS002203) doi: 10.1029/2020ms002203
- 939 Rasp, S., Pritchard, M. S., & Gentine, P. (2018, sep). Deep learning to represent
940 subgrid processes in climate models. *Proceedings of the National Academy*
941 *of Sciences of the United States of America*, 115(39), 9684–9689. Retrieved
942 from <https://gitlab.com/mspritch/spcam3.0-neural-net/tree/nn> doi:
943 10.1073/pnas.1810286115
- 944 Rasu, E., Bernstein, R., Huntingford, C., Jeffers, E. S., Bonsall, M. B., Christensen,
945 H. M., ... Yang, H. (2019). Machine learning and artificial intelligence
946 to aid climate change research and preparedness. *Environ. Res. Lett*, 14,
947 124007. Retrieved from <https://doi.org/10.1088/1748-9326/ab4e55> doi:
948 10.1088/1748-9326/ab4e55
- 949 Ruder, S. (2016, sep). An overview of gradient descent optimization algorithms.
950 *arXiv*. Retrieved from <http://arxiv.org/abs/1609.04747>
- 951 Samek, W., Binder, A., Montavon, G., Lapuschkin, S., & Müller, K. R. (2017).

- 952 Evaluating the visualization of what a deep neural network has learned.
953 *IEEE Transactions on Neural Networks and Learning Systems*, 28(11). doi:
954 10.1109/TNNLS.2016.2599820
- 955 Samek, W., Montavon, G., Lapuschkin, S., Anders, C. J., & Müller, K.-R. (2020,
956 mar). Toward Interpretable Machine Learning: Transparent Deep Neural
957 Networks and Beyond. *arXiv*. Retrieved from [http://arxiv.org/abs/](http://arxiv.org/abs/2003.07631)
958 2003.07631
- 959 Santer, B. D., Fyfe, J. C., Solomon, S., Painter, J. F., Bonfils, C., Pallotta, G., &
960 Zelinka, M. D. (2019, oct). Quantifying stochastic uncertainty in detection
961 time of human-caused climate signals. *Proceedings of the National Academy*
962 *of Sciences of the United States of America*, 116(40), 19821–19827. Retrieved
963 from www.pnas.org/cgi/doi/10.1073/pnas.1922907117
964 10.1073/pnas.1904586116
- 965 Schneider, T., & Held, I. M. (2001). Discriminants of twentieth-century changes
966 in earth surface temperatures. *Journal of Climate*, 14(3). doi: 10.1175/1520
967 -0442(2001)014<0249:LDOTCC>2.0.CO;2
- 968 Sherwood, S. C., Webb, M. J., Annan, J. D., Armour, K. C., Forster, P. M., Har-
969 greaves, J. C., ... Zelinka, M. D. (2020, dec). An Assessment of Earth's
970 Climate Sensitivity Using Multiple Lines of Evidence. *Reviews of Geophysics*,
971 58(4). Retrieved from [https://agupubs.onlinelibrary.wiley.com/doi/](https://agupubs.onlinelibrary.wiley.com/doi/full/10.1029/2019RG000678)
972 full/10.1029/2019RG000678 doi: 10.1029/2019rg000678
- 973 Sippel, S., Meinshausen, N., Fischer, E. M., Székely, E., & Knutti, R. (2020, jan).
974 *Climate change now detectable from any single day of weather at global scale*
975 (Vol. 10) (No. 1). Nature Research. doi: 10.1038/s41558-019-0666-7
- 976 Sippel, S., Meinshausen, N., Merrifield, A., Lehner, F., Pendergrass, A. G., Fischer,
977 E., & Knutti, R. (2019). Uncovering the forced climate response from a single
978 ensemble member using statistical learning. *Journal of Climate*, 32(17). doi:
979 10.1175/JCLI-D-18-0882.1
- 980 Slivinski, L. C., Compo, G. P., Sardeshmukh, P. D., Whitaker, J. S., McColl, C.,
981 Allan, R. J., ... Wyszyński, P. (2020, dec). An evaluation of the performance
982 of the 20th Century Reanalysis version 3. *Journal of Climate*, -1(aop), 1–64.
983 Retrieved from [https://journals.ametsoc.org/view/journals/clim/aop/](https://journals.ametsoc.org/view/journals/clim/aop/JCLI-D-20-0505.1/JCLI-D-20-0505.1.xml)
984 JCLI-D-20-0505.1/JCLI-D-20-0505.1.xml doi: 10.1175/JCLI-D-20-0505.1

- 985 Slivinski, L. C., Compo, G. P., Whitaker, J. S., Sardeshmukh, P. D., Giese, B. S.,
 986 McColl, C., ... Wyszyński, P. (2019, oct). Towards a more reliable historical
 987 reanalysis: Improvements for version 3 of the Twentieth Century Reanalysis
 988 system. *Quarterly Journal of the Royal Meteorological Society*, *145*(724),
 989 2876–2908. Retrieved from [https://onlinelibrary.wiley.com/doi/abs/](https://onlinelibrary.wiley.com/doi/abs/10.1002/qj.3598)
 990 [10.1002/qj.3598](https://onlinelibrary.wiley.com/doi/abs/10.1002/qj.3598) doi: 10.1002/qj.3598
- 991 Smith, C., Kramer, R., Myhre, G., Alterskjr, K., Collins, W., Sima, A., ... M.
 992 Forster, P. (2020). Effective radiative forcing and adjustments in CMIP6
 993 models. *Atmospheric Chemistry and Physics*, *20*(16). doi: 10.5194/
 994 acp-20-9591-2020
- 995 Smith, D. M., Booth, B. B., Dunstone, N. J., Eade, R., Hermanson, L., Jones, G. S.,
 996 ... Thompson, V. (2016). Role of volcanic and anthropogenic aerosols in the
 997 recent global surface warming slowdown. *Nature Climate Change*, *6*(10). doi:
 998 [10.1038/nclimate3058](https://doi.org/10.1038/nclimate3058)
- 999 Stocker, T. F., Qin, D., Plattner, G. K., Tignor, M. M., Allen, S. K., Boschung,
 1000 J., ... Midgley, P. M. (2013). *Climate change 2013 the physical sci-*
 1001 *ence basis: Working Group I contribution to the fifth assessment report*
 1002 *of the intergovernmental panel on climate change* (Vol. 9781107057). doi:
 1003 [10.1017/CBO9781107415324](https://doi.org/10.1017/CBO9781107415324)
- 1004 Stott, P. A., Mitchell, J. F., Allen, M. R., Delworth, T. L., Gregory, J. M., Meehl,
 1005 G. A., & Santer, B. D. (2006). Observational constraints on past attributable
 1006 warming and predictions of future global warming. *Journal of Climate*, *19*(13).
 1007 doi: 10.1175/JCLI3802.1
- 1008 Thorsen, T. J., Winker, D. M., & Ferrare, R. A. (2020, oct). Uncertainty in obser-
 1009 vational estimates of the aerosol direct radiative effect and forcing. *Journal of*
 1010 *Climate*, *34*(1), 1–63. Retrieved from [https://journals.ametsoc.org/view/](https://journals.ametsoc.org/view/journals/clim/34/1/jcliD191009.xml)
 1011 [journals/clim/34/1/jcliD191009.xml](https://journals.ametsoc.org/view/journals/clim/34/1/jcliD191009.xml) doi: 10.1175/jcli-d-19-1009.1
- 1012 Thyng, K., Greene, C., Hetland, R., Zimmerle, H., & DiMarco, S. (2016, sep). True
 1013 Colors of Oceanography: Guidelines for Effective and Accurate Colormap
 1014 Selection. *Oceanography*, *29*(3), 9–13. Retrieved from [https://tos.org/](https://tos.org/oceanography/article/true-colors-of-oceanography-guidelines-for-effective-and-accurate-colormap)
 1015 [oceanography/article/true-colors-of-oceanography-guidelines-for-](https://tos.org/oceanography/article/true-colors-of-oceanography-guidelines-for-effective-and-accurate-colormap)
 1016 [-effective-and-accurate-colormap](https://tos.org/oceanography/article/true-colors-of-oceanography-guidelines-for-effective-and-accurate-colormap) doi: 10.5670/oceanog.2016.66
- 1017 Toms, B. A., Barnes, E. A., & Ebert-Uphoff, I. (2020, sep). Physically Interpretable

- 1018 Neural Networks for the Geosciences: Applications to Earth System Vari-
1019 ability. *Journal of Advances in Modeling Earth Systems*, 12(9). Retrieved
1020 from <https://onlinelibrary.wiley.com/doi/10.1029/2019MS002002> doi:
1021 10.1029/2019MS002002
- 1022 Virtanen, P., Gommers, R., Oliphant, T. E., Haberland, M., Reddy, T., Courn-
1023 peau, D., ... Vázquez-Baeza, Y. (2020). SciPy 1.0: fundamental algo-
1024 rithms for scientific computing in Python. *Nature Methods*, 17(3). doi:
1025 10.1038/s41592-019-0686-2
- 1026 Vuuren, D. P., Edmonds, J., Kainuma, M., Riahi, K., Thomson, A., Hibbard,
1027 K., ... Rose, S. K. (2011, aug). The representative concentration path-
1028 ways: an overview. *Climatic Change*, 109(1-2), 5–31. Retrieved from
1029 <http://link.springer.com/10.1007/s10584-011-0148-z> doi: 10.1007/
1030 s10584-011-0148-z
- 1031 Wang, H., Xie, S., Zheng, X., Kosaka, Y., Xu, Y., & Geng, Y. (2020, oct). Dy-
1032 namics of Southern Hemisphere Atmospheric Circulation Response to Anthro-
1033 pogenic Aerosol Forcing. *Geophysical Research Letters*, 47(19). Retrieved
1034 from <https://onlinelibrary.wiley.com/doi/10.1029/2020GL089919> doi:
1035 10.1029/2020GL089919
- 1036 Watson-Parris, D. (2020, aug). Machine learning for weather and climate are worlds
1037 apart. *arXiv*. Retrieved from <http://arxiv.org/abs/2008.10679>
- 1038 Weyn, J. A., Durran, D. R., & Caruana, R. (2020, sep). Improving Data-Driven
1039 Global Weather Prediction Using Deep Convolutional Neural Networks
1040 on a Cubed Sphere. *Journal of Advances in Modeling Earth Systems*,
1041 12(9). Retrieved from [https://onlinelibrary.wiley.com/doi/10.1029/
1042 2020MS002109](https://onlinelibrary.wiley.com/doi/10.1029/2020MS002109) doi: 10.1029/2020MS002109
- 1043 Wills, R., Battisti, D. S., Armour, K. C., Schneider, T., & Deser, C. (2020, sep).
1044 Pattern Recognition Methods to Separate Forced Responses from Internal
1045 Variability in Climate Model Ensembles and Observations. *Journal of Climate*,
1046 33(20), 8693–8719. Retrieved from [https://doi.org/10.1175/JCLI-D-19-
1047 0855.1](https://doi.org/10.1175/JCLI-D-19-0855.1) doi: 10.1175/JCLI-D-19-0855.1
- 1048 Wills, R., Sippel, S., & Barnes, E. A. (2020). Separating forced and unforced
1049 components of climate change: The utility of pattern recognition methods
1050 in Large Ensembles and observations. *US CLIVAR Variations*, 18(2). doi:

1051 10.5065/0DSY-WH17

1052 Yoshioka, M., Regayre, L. A., Pringle, K. J., Johnson, J. S., Mann, G. W., Par-
1053 tridge, D. G., ... Carslaw, K. S. (2019). Ensembles of Global Climate Model
1054 Variants Designed for the Quantification and Constraint of Uncertainty in
1055 Aerosols and Their Radiative Forcing. *Journal of Advances in Modeling Earth*
1056 *Systems*, 11(11). doi: 10.1029/2019MS001628

1057 Zadeh, L. A. (1965, jun). Fuzzy sets. *Information and Control*, 8(3), 338–353. doi:
1058 10.1016/S0019-9958(65)90241-X

1059 Zanna, L., & Bolton, T. (2020, sep). Data-Driven Equation Discovery of Ocean
1060 Mesoscale Closures. *Geophysical Research Letters*, 47(17). Retrieved from
1061 <https://onlinelibrary.wiley.com/doi/10.1029/2020GL088376> doi:
1062 10.1029/2020GL088376

1063 Zelinka, M. D., Andrews, T., Forster, P. M., & Taylor, K. E. (2014, jun). Quan-
1064 tifying components of aerosol-cloud-radiation interactions in climate models.
1065 *Journal of Geophysical Research: Atmospheres*, 119(12), 7599–7615. Retrieved
1066 from [https://agupubs.onlinelibrary.wiley.com/doi/full/10.1002/](https://agupubs.onlinelibrary.wiley.com/doi/full/10.1002/2014JD021710)
1067 [2014JD021710](https://agupubs.onlinelibrary.wiley.com/doi/full/10.1002/2014JD021710) doi: 10.1002/2014JD021710